

CHARACTERIZATION OF URANIUM, URANIUM OXIDE AND
SILICON MULTILAYER THIN FILMS

by

David T. Oliphant

A thesis submitted to the faculty of

Brigham Young University

in partial fulfillment of the requirements for the degree of

Master of Science

Physics and Astronomy Department

Brigham Young University

December 2000

BRIGHAM YOUNG UNIVERSITY

GRADUATE COMMITTEE APPROVAL

of a thesis submitted by

David T. Oliphant

This thesis has been read by each member of the following graduate committee and by majority vote has been found to be satisfactory.

Date

R. Steven Turley, Chair

Date

David D. Allred

Date

Robert C. Davis

BRIGHAM YOUNG UNIVERSITY

As chair of the candidate's graduate committee, I have read the thesis of David T. Oliphant in its final form and have found that (1) its format, citations, and bibliographical style are consistent and acceptable and fulfill university and department style requirements; (2) its illustrative materials including figures, tables, and charts are in place; and (3) the final manuscript is satisfactory to the graduate committee and is ready for submission to the university library.

Date

R. Steven Turley, Chair

Accepted for the Department

Jean-Francois S. Van Huele
Graduate Coordinator

Accepted for the College

Earl M. Woolley
Dean, College of Physical
and Mathematical Sciences

ABSTRACT

CHARACTERIZATION OF URANIUM, URANIUM OXIDE AND SILICON MULTILAYER THIN FILMS

David T. Oliphant

Department of Physics and Astronomy

Master of Science

In order to understand discrepancies between calculated and measured values of reflectance for the IMAGE mirrors a characterization of the top layer of uranium was undertaken. To better understand this uranium oxide cap, single thin film layers of uranium were also studied. Physical and chemical properties of samples were studied with atomic force microscopy, X ray diffraction, X ray photoelectron spectroscopy, transmission electron microscopy and ellipsometry. It was determined that most of the uranium oxide cap is composed of uranium dioxide. However, there is a surface layer different than the pure dioxide. This layer is likely a hydroxide or hyperstoichiometric uranium oxide or both. It was also found that the bottom of the uranium oxide cap diffused into the amorphous silicon layer beneath it. Not far into the underlying silicon layer the uranium was found to stop oxidizing. A study of the oxidation rate

of sputtered uranium thin films was also conducted. It showed a rate that varied with time, dissimilar to published uranium oxidation rates for bulk samples. In addition, a new method for analyzing X ray diffraction data was also formulated.

ACKNOWLEDGMENTS

I am indebted to the members of my committee Dr. Turley, Dr. Allred and Dr. Davis. Their assistance and counsel in this research and thesis has not only improved the quality of this work but has also improved the quality of my life. I am also grateful for the many students who have helped. I am grateful to David Balogh and Matt Squires for their help in making the uranium thin film samples. Jennifer McBride at the University of Utah and Mike Standing at the TEM lab here at BYU were most valuable in helping with analyzing the thin films. Their unique skills and understanding of their instruments made much of this work possible.

I am also very grateful for the love and support of my family. My children Alison and Emily have been very accommodating in allowing Daddy to work on his “thesis”. My wife Leslie has often gone the extra mile in helping me to get this completed. Her editing and scientific skills as well as her moral support have made this all possible. I am grateful to God who has given me insight and direction in helping me understand His universe.

Although this work is not perfect, I have given it my best. I am reassured by the words of Aristotle: “It is the mark of an instructed mind to rest satisfied with the degree of precision which the nature of the subject permits and not to seek an exactness where only an approximation of truth is possible.”

Contents

1	Background	1
1.1	Introduction	1
1.2	Previous Work at BYU	3
1.3	Light Interacting With Matter	5
1.3.1	Abrupt Interfaces	8
1.3.2	Multilayer Reflectance	10
1.3.3	Non-Uniform Interfaces – Roughness and Diffusion	12
2	Characterization Methods	17
2.1	X Ray Diffraction	18
2.1.1	Theory	18
2.1.2	Experimental Setup	20
2.1.3	Traditional Analysis	21
2.1.4	Automated Analysis	24
2.2	Ellipsometry	31
2.2.1	Ellipsometry Theory	31
2.2.2	Experimental Setup	32
2.3	Transmission Electron Microscopy	33
2.3.1	TEM Theory	33
2.3.2	Small Angle Cleavage Technique	34
2.4	X Ray Photoelectron Spectroscopy	37
3	Results	40
3.1	Depth Profile	41
3.1.1	Atomic Force Microscopy	41
3.1.2	X Ray Diffraction	43
3.1.3	Transmission Electron Microscopy	48
3.1.4	X Ray Photoelectron Spectroscopy	48
3.2	Optical Constants	58
3.3	Oxidation Rates	60
3.3.1	Units	60
3.3.2	Previous Work	65
3.3.3	Ellipsometry Measurements	66

4 Conclusion	70
A XRD $P_c(d_1, d_2)$ Surface plots	73

List of Tables

1.1	Interface Profile Functions (IPF) and Corresponding $\tilde{w}(s_i), \sigma = \text{rms}$ roughness.	15
3.1	Summary of XRD Measurements of Single Layer Uranium Samples. .	44
3.2	Summary of ellipsometry measurements used for determining optical constants of uranium oxide, all thicknesses in Å. Time is time from removing from vacuum.	63
3.3	Expansion ratios of different uranium oxides.	65

List of Figures

1.1	EUV Imager First Photo.	2
1.2	Light Incident On a Boundary.	9
1.3	Multilayer thin film with a total of $x - 1$ layers on top of the substrate. Each layer represents a material. The boundaries between different materials cause reflection.	11
2.1	XRD data plotted on a normalized linear scale.	22
2.2	XRD data plotted on a normalized log scale.	23
2.3	Comparison of reflection off a multilayer, D_r , and reflection off a bulk sample, B_c	27
2.4	Modified XRD Data.	28
2.5	d_1 and d_2 space for a uranium/aluminum multilayer.	30
2.6	Four wedge-shaped samples mounted on a single hole TEM grid[17].	37
2.7	XPS scan of U8Si157.	39
3.1	AFM surface image and analysis for U66. Lighter areas are higher parts, dark areas are lower.	42
3.2	AFM surface image and analysis for U68B180. Lighter areas are higher parts, dark areas are lower.	43
3.3	d and Γ space for U8Si157. Dark horizontal line near the top represents a d -spacing of 187 Å, other curved lines represent possible Γ values.	45
3.4	d_1 and d_2 space for U8Si157.	46
3.5	TEM image of U8Si157.	47
3.6	XPS data for 4f uranium doublet. Comparison of old (U8Si157), annealed (U67B180) and fresh (U67C) samples.	50
3.7	XPS data for oxygen 1s. Comparison of old (U8Si157), annealed (U67B180) and fresh (U67C) samples.	51
3.8	XPS depth profile data for U4f doublet. Time represents sputter time for removing surface layers and corresponds to depth.	53
3.9	XPS depth profile data for oxygen 1s. Time represents sputter time for removing surface layers and corresponds to depth.	55
3.10	Transition from uranium to silicon. XPS depth profile data for U5d3, Si2p, U5d5. Silicon peak is in the center at about 100 eV. The two uranium peaks are on either side of the silicon peak. Time represents sputter time for removing surface layers and corresponds to depth.	56

3.11	Transition from uranium oxide to uranium. XPS depth profile data for U4f doublet. Time represents sputter time for removing surface layers and corresponds to depth.	57
3.12	Hypothetical depth profile of uranium oxide cap on U8Si157.	59
3.13	Real part of the index of refraction for uranium oxide. Comparison of values for uranium dioxide found by Ackermann to values determined in this study with ellipsometry.	61
3.14	Imaginary part of the index of refraction for uranium oxide. Comparison of values for uranium dioxide found by Ackermann to values determined in this study with ellipsometry.	62
3.15	Uranium Oxidation Data and Fit: $y = 12.5x - 31$ $x = \ln t$	68
A.1	d_1 and d_2 space for a hypothetical multilayer with a d-spacing of 130 Å and a Γ of 0.7.	74
A.2	d_1 and d_2 space for a hypothetical multilayer with a d-spacing of 130 Å and a Γ of 0.2.	75
A.3	d_1 and d_2 space for a ruthenium/aluminum multilayer with 4 periods.	76

Chapter 1

Background

1.1 Introduction

On May 5, 2000 the extreme ultraviolet imager on the IMAGE satellite sent back to earth its first pictures taken using specially designed soft X ray mirrors (figure 1.1). The IMAGE mission will increase our understanding of the electromagnetic weather around the earth. Geomagnetic storms brought on by solar activity can adversely affect orbiting satellites, communications, large electrical grids and other electronic equipment. By using a number of different instruments, including the EUV imager, the IMAGE satellite collects data about the plasmasphere around the earth. Under the direction of Bill R. Sandel, the University of Arizona's Lunar and Planetary Laboratory built the EUV imager for the IMAGE mission [1]. They asked Dr. David Allred and the EUV group at BYU to design and make the mirrors for the EUV imager.

The mirrors' multi-functional design is unique. They reflect 304 \AA wavelength light well but have a low reflectance at 584 \AA . This allows the IMAGE satellite to image the He ions around the earth without being saturated by the bright light from

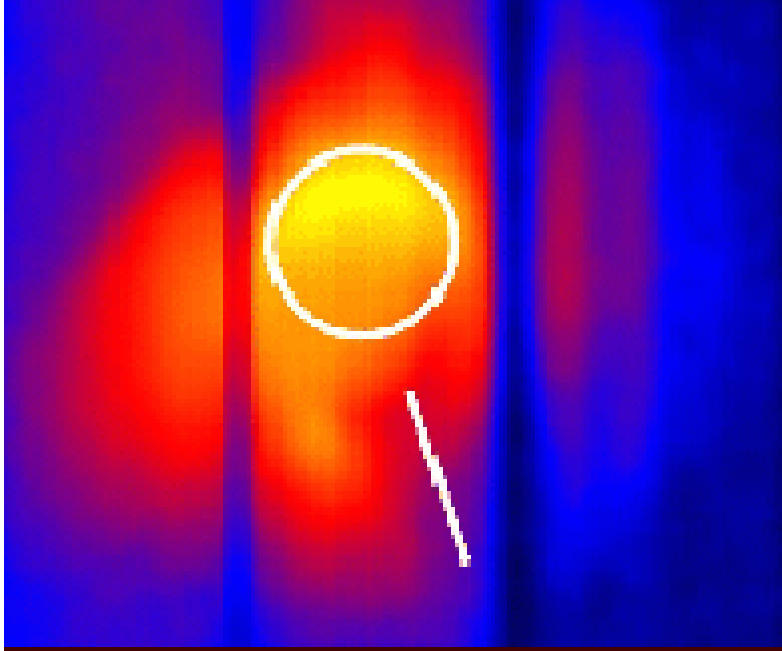


Figure 1.1: EUV Imager First Photo.

neutral helium [2]. Surprisingly the mirrors worked better than expected. With what was known about the multilayer mirrors at the time they should reflect 29% [3] of the light at 304 \AA and about 3% at 584 \AA . The measured reflectance at 304 \AA was 23%, a large discrepancy but not nearly as large as the factor of 3 at 584 \AA . Its measured reflectance was about 1% [3]. There was clearly something important about the nature of the multilayer mirror that was not understood. In the process of designing and producing the mirror it was found experimentally that a thin layer of oxidized uranium deposited on the top of the multilayer gave the best reflectance values.

In order to understand the discrepancy in reflectance, a complete characterization of the uranium oxide cap needed to be conducted. This thesis outlines research

completed on both the physical and chemical properties of thin films of oxidized uranium and multilayers of oxidized uranium on uranium and amorphous silicon. Thickness has been analyzed with X ray diffraction (XRD), transmission electron microscopy (TEM) and ellipsometric measurements. Although sputter rates for the uranium were previously calculated, the amount of expansion due to oxidation was unknown. For this reason a study of the oxidation rates and the oxidation process of uranium is also outlined. Atomic force microscopy (AFM) was used as a direct measurement of surface roughness. Roughness was also included in the models used for reflection measurement. X ray photoelectron spectroscopy (XPS) was used to better understand the elemental composition and chemical binding of the multilayers.

1.2 Previous Work at BYU

The design and fabrication of the EUV IMAGE mirrors presented a number of challenges. First, it is difficult to get a large contrast in optical constant between materials in the EUV. Optical constants of different materials in the EUV are very similar. This makes the reflectance from a single interface very small. Another serious challenge is with oxidation. Oxygen is extremely absorptive at 584 \AA , the wavelength of light the mirror needed to reflect. Too thick of a layer of oxide on the top of the mirror could completely destroy the desired properties of the multilayer. Another problem is the dependability of optical constants in this region of the spectrum; published values often conflict [3]. In addition, the role that chemical bonding has on the optical constants in the EUV region is not well understood.

The problem of low reflectance at each interface is typically overcome by having many periods in the multilayer so that there are many boundaries to contribute to the reflectance. However, large absorptive constants limit the number of layers. Each period is typically composed of a bi-layer, two materials one on top of the other. A multilayer is made by staking a number of these periods on top of each other. Standard X ray mirror design practice says that the period should be composed of a relatively thin layer of material with a large absorptive constant and the rest of the period being composed of a less absorptive spacer material. Shannon Lunt[4] developed a computer program to find the best combination of materials and the thicknesses for each of the layers. Lunt's software uses a combination of the Genetic Algorithm, a global optimization procedure, and a local minimization technique called the Simplex Method. It has the flexibility to allow for aperiodic layers. The optimum mirror design found by Lunt's software that met the specifications for the IMAGE mission was an aperiodic Y_2O_3 and Al multilayer with a total of 16 layers.

Y_2O_3 is not a conductor and could not be sputtered using DC magnetron sputtering. This made it impractical to use Y_2O_3 because BYU was not equipped for RF sputtering. Uranium/aluminum multilayers were produced instead. These multilayers were studied by Adam Fenimore [5]. He found that the aluminum oxidizes deep into the stack, producing a thick layer of oxide. In addition, he found significant columnar growth. These were unacceptable because they destroyed the desired optical properties.

Upon review of the published optical constants in the EUV region it was found

that there is disagreement between sources. Matthew Squires' study of the optical constants of uranium and silicon found that chemical bonding may affect the values of the optical constants in the EUV region [3]. Squires used a McPherson hollow cathode plasma lamp with He gas to produce EUV light at 304 Å and 584 Å. His reflectance measurements of uranium and silicon multilayers at these wavelengths shows that further research needs to be conducted to obtain accurate and reliable optical constants in the EUV.

The final mirrors were made with uranium and silicon. Aperiodic multilayers were found to be too difficult to analyze with X ray diffraction. For this reason periodic structures were adopted. The multilayers consisted of 7 bilayers with a period thickness, or d-spacing, of 181 Å and a ratio of thicknesses within the period (Γ) of about 0.7 with the silicon layer on the top of the period [6]. If the silicon was left on top it would oxidize and dramatically change the reflectance. To avoid this a thin layer of uranium was deposited on top and allowed to oxidize. The addition of this uranium oxide cap worked very well. This cap not only prevented the silicon from oxidizing but it also enhanced the desired reflectance properties.

1.3 Light Interacting With Matter

Ellipsometry and X ray diffraction, as well as other characterization tools, use reflectance data to better understand a sample. For this reason the method for calculating reflectance from a multilayer is outlined here. Information more specific to the characterization technique will be discussed in chapter 2.

The mathematics of light is described by using Maxwell's equations and the appropriate boundary conditions. Assuming homogeneous and isotropic media Maxwell's equations can be written as[7]

$$\nabla \cdot \mathbf{E} = \frac{\rho}{\epsilon} \quad (1.1)$$

$$\nabla \cdot \mathbf{B} = 0 \quad (1.2)$$

$$\nabla \times \mathbf{E} = -\frac{d\mathbf{B}}{dt} \quad (1.3)$$

$$\nabla \times \mathbf{B} = \mu\epsilon\frac{d\mathbf{E}}{dt} + \mu\mathbf{J}. \quad (1.4)$$

In free space $\mathbf{J} = 0$, $\rho = 0$, $\epsilon = \epsilon_0$ and $\mu = \mu_0$. Taking the cross product of equation 1.3 and using equation 1.2 and 1.4 leads to the wave equation for \mathbf{E} :

$$\nabla^2\mathbf{E} = -\mu\epsilon\frac{d^2\mathbf{E}}{d^2t} \Rightarrow \mathbf{E} = \mathbf{E}_0e^{i(\mathbf{k}\cdot\mathbf{x}-\omega t)}. \quad (1.5)$$

If the same thing is done with equations 1.4, 1.1 and 1.3 the wave equation for \mathbf{B} is derived.

$$\nabla^2\mathbf{B} = -\mu\epsilon\frac{d^2\mathbf{B}}{d^2t} \Rightarrow \mathbf{B} = \mathbf{B}_0e^{i(\mathbf{k}\cdot\mathbf{x}-\omega t)}, \quad (1.6)$$

where the wave number \mathbf{k} is defined as

$$\mathbf{k} \equiv \omega\sqrt{\mu\epsilon}\hat{\mathbf{k}} \quad (1.7)$$

The velocity of this wave is given by

$$v = \frac{1}{\sqrt{\mu\epsilon}}. \quad (1.8)$$

When the wave is propagating in free space $v = c$, the speed of light in vacuum.

In optics it is common to define the optical constant n for a material at a given frequency as the ratio of the speed of light in a vacuum to the speed of light in that material.

$$n = \frac{c}{v} \quad (1.9)$$

With equation 1.8, n can be written as

$$n = \sqrt{\frac{\mu\epsilon}{\mu_0\epsilon_0}} \quad (1.10)$$

It is also common to define the relative permeability μ and the relative permittivity ϵ as being the ratios of μ and ϵ to their vacuum values μ_0 and ϵ_0 . In addition, the materials discussed in this thesis have a relative permeability very close to one. This makes it a very good approximation to describe the index of refraction as just the square root of the relative permittivity ($n = \sqrt{\epsilon}$) [8]. This allows us to discuss the optical properties of a material by just looking at the relative permittivity ϵ .

The permittivity of a material depends on the electrons' energy levels within the atom. The bound electrons can be thought of as damped simple harmonic oscillators especially when they interact with X rays. If each electron within an atom has a natural frequency of ω_j , a damping constant of γ_j with an oscillator strength of f_j , then the relative permittivity can be modeled as

$$\epsilon(\omega) = 1 + \frac{Ne^2}{\epsilon_0 m} \sum_j f_j (\omega_j^2 - \omega^2 - i\omega\gamma_j)^{-1}, \quad (1.11)$$

where N is the number of molecules per unit volume and e and m are the charge and mass of an electron, respectively [7]. The summation accounts for all the electrons within the atom. The damping term γ_j in equation 1.11 translates into an imaginary term in the index of refraction. When the complex index of refraction $n = (n_r + in_i)$ is used the wave number can then be defined as

$$\mathbf{k} = \frac{2\pi}{\lambda_0} n \hat{\mathbf{k}} = \frac{2\pi}{\lambda_0} (n_r + in_i) \hat{\mathbf{k}} \quad (1.12)$$

where λ_0 is the vacuum wavelength of the light. If this \mathbf{k} is employed in the wave equations for \mathbf{E} it is clear to see that the wave is damped as it propagates.

$$\mathbf{E} = \mathbf{E}_0 e^{i(\frac{2\pi}{\lambda_0} (n_r + in_i) \hat{\mathbf{k}} \cdot \mathbf{x})} = \mathbf{E}_0 e^{i(\frac{2\pi}{\lambda_0} n_r \hat{\mathbf{k}} \cdot \mathbf{x})} e^{-\frac{2\pi}{\lambda_0} n_i \hat{\mathbf{k}} \cdot \mathbf{x}} \quad (1.13)$$

This formalism works well for describing complicated quantum mechanical interactions of light with matter.

1.3.1 Abrupt Interfaces

To calculate the total reflectance of a multilayer mirror it is necessary to know what happens at a single interface between two different materials. This is done by using the boundary conditions for the electric and magnetic fields to match up the waves on each side of the boundary. The tangential component of the electric field (E_{\parallel}) and the normal component of the magnetic field (B_{\perp}) are continuous across an interface. On the other hand the normal component of the electric field (E_{\perp}) and the tangential component of the magnetic field (B_{\parallel}) are discontinuous at a boundary due to the charge and current at the boundary. Applying these boundary conditions to an

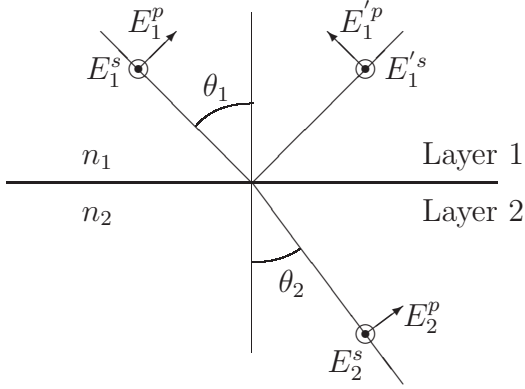


Figure 1.2: Light Incident On a Boundary.

electromagnetic wave incident on an interface at an angle of θ_1 leads to Snell's law:

$$n_1 \sin(\theta_1) = n_2 \sin(\theta_2), \quad (1.14)$$

where θ_2 is the angle between the normal and the transmitted wave, and n is the index of refraction. When n is complex the angles no longer represent physical angles.

The ratio of the reflected electric field (E'_1) to the incident electric field (E_1) of an electromagnetic plane wave incident on the boundary between layer 1 and layer 2 is given by the Fresnel equations [8].

E perpendicular to the optical plane (s polarization):

$$r_{12}^s \equiv \frac{E_1'^s}{E_1^s} = \frac{n_1 \cos(\theta_1) - n_2 \cos(\theta_2)}{n_1 \cos(\theta_1) + n_2 \cos(\theta_2)} \quad (1.15)$$

E parallel to the optical plane (p polarization):

$$r_{12}^p \equiv \frac{E_1'^p}{E_1^p} = \frac{n_1 \cos(\theta_2) - n_2 \cos(\theta_1)}{n_1 \cos(\theta_2) + n_2 \cos(\theta_1)} \quad (1.16)$$

The transmission Fresnel equations are not included here. A more detailed explanation of the derivation of the Fresnel equations can be found in any number of optics

books [7, 8, 9].

1.3.2 Multilayer Reflectance

Calculating the reflectance for a multilayer combines the effects of reflection off each boundary with the way the electric field is modified as it is transmitted through each layer. The formalism presented below is from the documentation with David Windt's computer program IMD[10]. Born and Wolf use a similar formalism [9]. It involves starting at the bottom-most boundary (the boundary between Layer # 0 and Layer # 1 in figure 1.3) to calculate the Fresnel coefficients. Here there is no reflected wave from lower boundaries, just an incident, reflected and transmitted wave. To account for the phase change as the wave propagates in the next layer up (Layer #1) the reflected electric field is modified by the phase factor:

$$e^{2i\beta_j}, \quad (1.17)$$

where

$$\beta_j = \frac{2\pi d_j n_j \cos(\theta_j)}{\lambda_0}, \quad j = 1, \quad (1.18)$$

and where λ_0 is the vacuum wavelength, d_j is the thickness of the j^{th} layer and n_j is the index of refraction for the j^{th} layer. Because n is complex, this equation not only accounts for the change in phase but also accounts for the absorption of the layer. At the next boundary (the boundary between Layer # 1 and Layer # 2) the reflection (the wave traveling up in Layer # 2) is calculated by the equation:

$$r_i = \frac{r_{ij} + r_j e^{2i\beta_j}}{1 + r_{ij} r_j e^{2i\beta_j}}, \quad i = 2, j = 1 \quad (1.19)$$

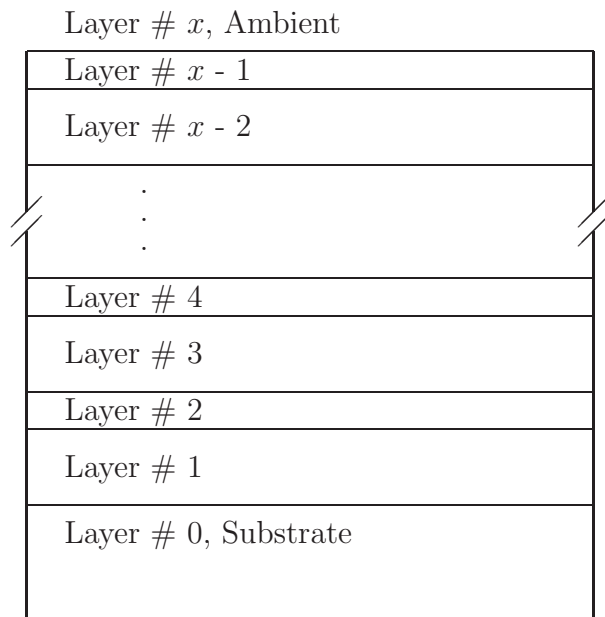


Figure 1.3: Multilayer thin film with a total of $x - 1$ layers on top of the substrate. Each layer represents a material. The boundaries between different materials cause reflection.

Here r_{ij} is one of the Fresnel coefficients, equations 1.16 or 1.15 depending on the polarization, and r_i and r_j are the reflected electric field ratio for the given layer. Equation 1.19 is then applied recursively ($i = 3, 4, 5 \dots x, j = 2, 3, 4, \dots x - 1$) until the top boundary is reached. At this point r_x gives the ratio of the total reflected electric field to the initial incident electric field. The fraction of the energy reflected is then given by

$$R = |r_x|^2. \quad (1.20)$$

This process is applied for both the s and p polarizations separately. The total non-polarized fraction of the energy reflected is given by the average of the reflection for the two polarizations.

$$R_{\text{total}} = \frac{R^p + R^s}{2} = \frac{|r_x^p|^2 + |r_x^s|^2}{2}. \quad (1.21)$$

1.3.3 Non-Uniform Interfaces – Roughness and Diffusion

It is impractical and unnecessary to completely describe the structure of a rough surface for calculating reflection and transmission values. A few statistics about the surface are usually sufficient. The most common statistic for describing a rough surface is the root-mean-square (rms roughness). This value is defined by the following:

$$\text{rms} = \sqrt{\frac{\sum_{i=1}^N (z_i - \bar{z})^2}{N}}, \quad (1.22)$$

where z_i is the height of the surface at the point i , \bar{z} is the average height over all measured points and N is the number of points. The rms value does not give any information about the lateral size of the structures that make up the roughness. It is

also highly dependent on the following measurement parameters [11]:

1. The length of the part of the sample being measured
2. The lateral resolution of the measuring tool
3. The lateral step size, i.e. the distance between measurements.

These measurement parameters are always a limiting factor in determining the roughness of a surface. Collectively they make the measurements “band limited.”

The power-spectral-density (PSD) function provides detail about the lateral size of structures making up the roughness. It is the square of the Fourier Transform of the surface profile. There are many other statistics to describe the roughness of a surface such as the height distribution function, the slope distribution function, the autocovariance function and others. Consult reference [11] for more information on these, the PSD function and the rms value.

For surfaces where the average lateral size of the roughness is much smaller than the wavelength of light that is being reflected roughness has the same effect as diffusion. For this scenario both diffusion and roughness can be modeled the same way. To model an interface between materials with dielectric constants ϵ_0 and ϵ'_0 , Stearns uses the interface profile function [12]:

$$p(z) \equiv \frac{1}{\Delta} \frac{\int \int [\epsilon(\mathbf{x}) - \epsilon'_0] dx dy}{\int \int dx dy}, \quad (1.23)$$

where $\Delta \equiv \epsilon_0 - \epsilon'_0$ and $\epsilon(\mathbf{x})$ describes the spatial variation of the dielectric function across the interface. The function $p(z)$ is just $\epsilon(\mathbf{x})$ averaged over x and y . In this way

it describes how the dielectric function varies in the z direction across the interface.

The derivative of $p(z)$ is then taken with respect to z to give $w(z)$:

$$w(z) = \frac{dp(z)}{dz}. \quad (1.24)$$

The Fresnel coefficients are then modified by multiplying them by $\tilde{w}(s_i)$, the Fourier transform of $w(z)$.

$$r'_{ij} = r_{ij}\tilde{w}(s_i), \quad s_i = \frac{4\pi \cos(\theta_i)}{\lambda} \quad (1.25)$$

where λ is the vacuum wavelength divided by the index of refraction. This is done for both p and s polarizations independently. These modified Fresnel coefficients are used in place of the normal Fresnel coefficients in equation 1.19. Stearns offers four examples of possible interface profile function and their corresponding $\tilde{w}(s_i)$. He mentions how three of them can be used to model different types of diffusion and roughness (see Table 1.1).

This method developed by Stearns is a first order approximation and is valid when

$$\frac{\Delta}{(n_z^0)^2} \ll 1. \quad (1.26)$$

Here n_z^0 is the z component of the incident wave vector. This condition holds when the difference between the dielectric constants of the two materials is small and when the incident wave is not too near grazing. In other words it holds when there is little reflectance off each interface, a condition common in the X ray region but not as applicable in the EUV.

Stearns' model does not take into account non-specular scattered light that upon further reflections gets scattered back into the specular field. It also only holds for

Table 1.1: Interface Profile Functions (IPF) and Corresponding $\tilde{w}(s_i)$, $\sigma =$ rms roughness.

IPF Name	$p(z)$	$\tilde{w}(s_i)$	model for
Error Function	$\frac{1}{\sqrt{\pi}} \int_{-\infty}^z e^{-\frac{t^2}{2\sigma^2}} dt$	$e^{-\frac{\sigma^2 s^2}{2}}$	classical diffusion
Linear	$0, z < -\sqrt{3}\sigma$ $\frac{1}{2} + \frac{z}{2\sqrt{3}\sigma}, z \leq \sqrt{3}\sigma$ $1, z > \sqrt{3}\sigma$	$\frac{\sin(\sqrt{3}\sigma s)}{\sqrt{3}\sigma s}$	diffusion due to sputtering
Exponential	$\frac{1}{2}e^{-\frac{\sqrt{2}z}{\sigma}}, z \leq 0$ $1 - \frac{1}{2}e^{-\frac{\sqrt{2}z}{\sigma}}, z > 0$	$\frac{1}{(1 + \frac{s^2\sigma^2}{2})}$	roughness

roughness on the length scale much smaller than a wavelength. For this reason an attempt was made to model roughness with a Monte Carlo ray tracing algorithm. We had hoped that such a model would help explain discrepancies in X ray diffraction data. The model was flawed because it did not fully account for the quantum mechanical nature of the photon. It was also deemed unnecessary because the condition of low reflectance at each interface in Stearns' model holds extremely well for X ray diffraction in the range (0.5° to 5° from grazing), the range for the data in question. The condition for the length scale is not satisfied as well. Taking this into account could be a topic of further research.

Diffusion can be modeled in a simpler, more accurate, but computationally more intensive way. This is done by breaking up a single interface into many layers. The

layers' index of refractions are a combination of the indices of the two materials that make up the single interface. Indices are weighted according to their position in the interface transition and the profile of that transition. To be accurate the thickness of each effective layer should be small compared to a wavelength. If, in addition, the total interface thickness is large this can mean there are many effective layers for each interface. If the multilayer has many interfaces the total number of effective layers can be huge. This makes the time it takes to compute the reflectance very long and impractical.

Chapter 2

Characterization Methods

There are many different methods for probing the compositional and/or structural nature of thin films. These can be categorized by what they use to probe the thin film and what they analyze. Both X ray diffraction and ellipsometry use photons to probe and photons to analyze thin films. On the other hand, X ray photoelectron spectroscopy and Auger spectroscopy use photons to probe but analyze the electrons that are emitted as a result of the incident X ray photons. Transmission electron microscopy as well as electron diffraction use electrons to probe and electrons to analyze. Secondary ion mass spectroscopy uses ions to probe and the atoms emitted from ion sputtering to analyze. Each method has its advantages and weaknesses. Some are better at compositional analysis. Others are better for structural analysis. Most can give information about both. For the work reported in this thesis X ray diffraction and ellipsometry were used for determining thicknesses. However, X ray diffraction can be used to infer composition when the material is crystalline. In

addition, by using ellipsometry to determine the index of refraction, information can be learned about the compositional nature of a thin film. Using data concurrently from a number of different methods for the same thin film can give a wealth of information about a sample. This chapter describes four methods and the way they were used to characterize uranium/silicon thin films. Other methods such as atomic force microscopy and secondary ion mass spectroscopy were also used but not as extensively as those described in this chapter.

2.1 X Ray Diffraction

2.1.1 Theory

X ray diffraction (XRD) is most commonly used to determine the distance between planes in crystals. Each plane will scatter X rays in the same way. So the phase change in the scattered waves is only a function of the separation between the planes, the angle of incidence, and the material. Constructive interference between scattered waves is described by Bragg's law [13]:

$$2d \sin(\theta) = n\lambda \tag{2.1}$$

Here θ is measured from grazing and n is the order of the peak, a positive integer. The incident X rays are scanned over a range of θ to find all the Bragg angles. For crystals where the spacing is on the order of a few angstroms only a few constructive interference peaks are observed. The amount of scattering of an X ray from a single crystal plane is small. However, in a bulk sample there are millions of crystal planes

that contribute to reflection. Therefore, the intensity of the constructive interference peaks is typically large. This makes it possible to observe peaks even at high angles. By knowing the position of each peak, Bragg's Law can be used to determine d , the spacing between planes.

$$d = \frac{(n_i - n_j)\lambda}{2[\sin(\theta_i) - \sin(\theta_j)]}, \quad (2.2)$$

where n_i and n_j are the order of the Bragg angles θ_i and θ_j respectively.

Multilayer thin films have some similarities to crystals. Periodic structures within a multilayer can produce Bragg-like peaks. For this reason a similar method can be employed for thin films. However, there are a few important differences. Even the largest of multilayers do not contain millions of separate layers like a crystal. For this reason the reflection off each interface becomes more important. XRD peaks from thin films can only be seen at angles near grazing where the X rays reflect well at each boundary. Also the thickness of each layer in a thin film is on the order of a few nanometers instead of a few angstroms. This increases the number of peaks that can be observed. Another important difference is due to the variety of index of refractions that a thin film can have. Some boundaries may introduce a phase change where others will not. This makes it so that where there would have been a peak just using equation 2.1 there may be a minimum. In addition, not all multilayers are periodic. To my knowledge, methods for analyzing aperiodic multilayers with XRD have not yet been fully researched.

To determine the thickness of a single layer an approximation can be made. At low angles, $\sin(\theta) \approx \theta$. If $n_i - n_j = 1$, i.e. if i and j are adjacent peaks, and if they

are both at low angles then equation 2.2 can be approximated with

$$d \approx \frac{\lambda}{2(\theta_i - \theta_j)} = \frac{\lambda}{2\Delta\theta} \quad (2.3)$$

The period ($\Delta\theta$) can be determined using peaks or minima. In this way it is not necessary to know the order of each peak or minima to get a good approximation for the thickness of the single layer. This same method can be applied to multilayers, but it is often more difficult to distinguish the value of $\Delta\theta$. There are many other periodic structures in the XRD data that are a result of the thicknesses of individual layers rather than the total period thickness. This method offers little help in determining structures for aperiodic multilayers. In addition this method is only an approximation. It does not account for the details of reflections off interfaces as described in section 1.3. For these reasons other methods are used for determining the structure of multilayers from XRD data. Some of these methods are discussed in sections 2.1.3 and 2.1.4.

2.1.2 Experimental Setup

A Scintag X ray diffractometer was used to collect XRD data for a number of different samples. Samples are mounted on a stationary sample holder. The angle of the source and detector arms are varied simultaneously. The Cu $K\alpha$ (1.54 Å, 8 k eV) radiation emitted from the X ray tube passes through a scatter slit, a collimator and a divergence slit before reaching the sample. On the detector side the light passes through another scatter slit, collimator and divergence slit before it reaches the detector. The slit sizes can be changed. Available slit sizes range from 6 mm to

0.05 mm. The slits and the collimator are designed to reduce the amount of non-specular light that reaches the detector. The slit size also affects the size of the X ray beam that reaches the sample. If a large divergence slit is used at very low angles ($\theta < 1^\circ$), the spot size of the beam on the sample can be larger than the sample itself. This makes it look like the reflectance at low angles drops off. However, the reflectance actually approaches unity as the angle goes to zero. The size of the slits also affects the intensity of the light that reaches the detector.

2.1.3 Traditional Analysis

X ray diffraction data is used to determine the period thickness (d) and the ratio(Γ) of the thicknesses of the top layer within a period to the period thickness. Past attempts to find d and Γ from the data with an automated computer program have not worked well. Global optimizers tend to find incorrect values and local optimizers tend to not converge well. Previously, XRD data from thin films at BYU has been fitted by visual comparison. The data is imported into a software package such as IMD [10] or wfit [14]. These programs plot the data alongside calculated values. The parameters for the calculated values are adjusted by the user until the two plots look similar. Then the d and Γ parameters are said to be a correct match to the data. Often it is difficult to tell when the two plots line up the best. The d spacing is easier to determine than Γ ; but other parameters such as inter-diffusion, slight variations in period, and different normalization make it extremely difficult for a trained user and nearly impossible for an untrained user to use this method.

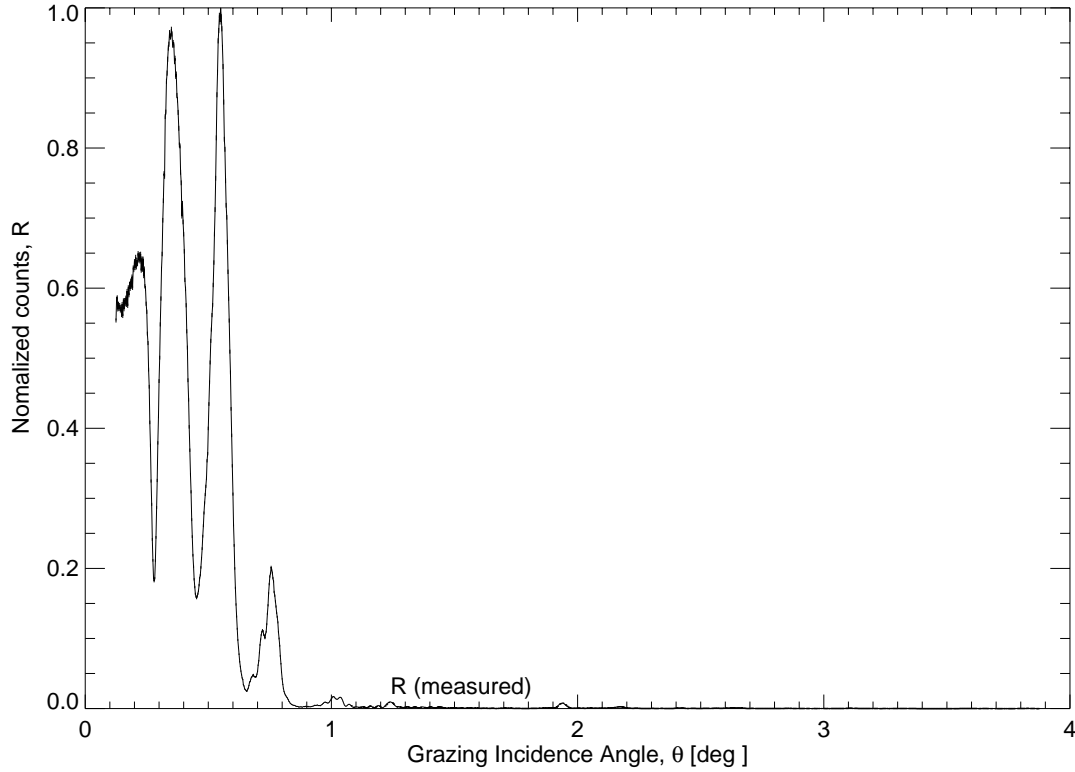


Figure 2.1: XRD data plotted on a normalized linear scale.

There are a few things that can make it easier to find a correct match. First, data is observed over a large range of θ (0° to 5° or so). Details of the data are more easily seen when plotted on a logarithmic scale (compare figure 2.1 to figure 2.2). Next, the period thickness is fit by lining up peaks and valleys in the plot of the data with peaks and valleys in the calculated plot. Another trick that can be helpful in fitting d spacing is to count the number of peaks within a certain range and make sure that number is the same in the calculated plot. Once d is established, Γ is fit by comparing the peak heights.

A slight misalignment in the X ray diffractometer when taking the data can make

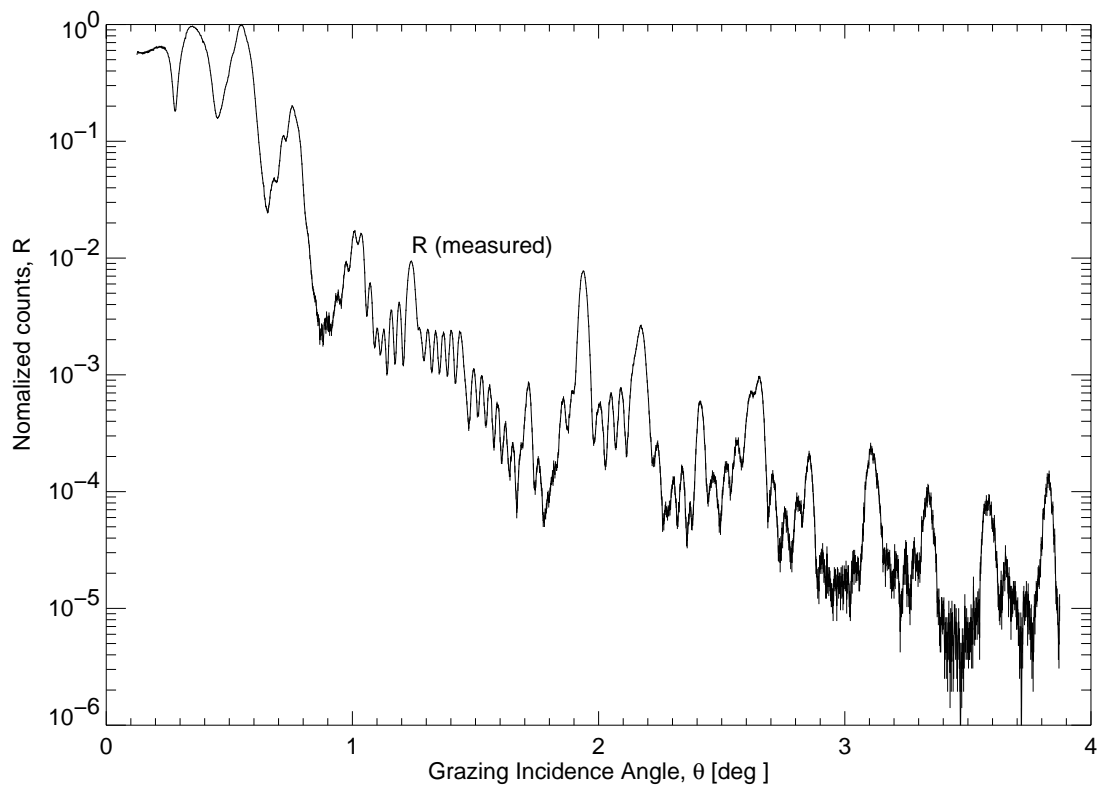


Figure 2.2: XRD data plotted on a normalized log scale.

this process even more difficult. Small misalignments will shift the θ axis by the amount that the instrument is off. It will also dramatically affect the intensities at very low angles ($\theta < 0.5$ from grazing). This should be considered carefully when fitting the data. Even for someone who is experienced at fitting XRD data visually, it is still difficult to quantify the quality of a fit. It can also be very time consuming to make a complete scan over the entire range of d and Γ . For these reasons I have developed a more automated method for analyzing this kind of data.

2.1.4 Automated Analysis

General Fitting Considerations

When fitting any kind of data there are generally four questions to ask.

1. Exactly what parameters is the fit trying to find?
2. What is being compared to the calculated values, the raw data, or some modified version?
3. How is the data being compared? (i.e. What is the merit function)? The most common merit function when comparing data is least squares (LS), or some modification of it. This involves taking the square of the difference between the data, $D(x)$, and the calculated values, $C(x)$, at each x and then summing up over all the data points.

$$LS = \sum_x (D(x) - C(x))^2 \tag{2.4}$$

Sometimes to get a number that is more meaningful when comparing different data sets, this value is divided by the total number of points. A small least squares value is better than a large one. However, it is difficult to tell precisely how good or how bad a fit is by looking at the least squares value.

4. How are the extrema found? There have been many methods developed to address this question. Methods such as the simplex method, Marquardt-Levenberg fitting algorithm, gradient method, and even the genetic algorithm, to name a few, are highly-developed, often-used fitting methods.

Admittedly the first three questions could be combined into one by having the merit function absorb the mathematics of the first two. However, it is beneficial to take a closer look at how the first two questions could be answered differently than usual.

New Fitting Method

In developing a more automated method, I have focused my attention on the first three things to consider, and specifically on the second of the four, the way the data is modified. Rather than having the computer find the extrema for the last consideration, a plot is made of the parameter-merit function space so the user can easily spot the maximum. The user may also learn other characteristics about the thin film by observing other features in the parameter-merit function space.

The values Γ and d are common nomenclature for describing the thickness properties of thin films. However, there are many other sets of numbers that are equivalent.

Another equivalent way to describe a thin film is with d_1 , the thickness of the top layer within a period, and d_2 the thickness of the bottom layer within a period. Other equivalent sets include d , d_1 and d , d_2 . It was found that by using d and Γ for parameter-merit function space it was easier to see what the d spacing was. However, by looking at the d_1 , d_2 parameter-merit function space other features in the plot were more interpretable. More work could be done to determine what parameters are the best to use for learning specific information.

The way the data was fit visually was considered for determining how the data should be modified before it is compared to calculated values. Using the raw data without modification weights the data at angles closer to grazing more heavily than the rest. This is because the reflectivity of most thin films at Cu $K\alpha$ radiation is extremely small except at angles very close to grazing. By not modifying the raw data, problems due to small misalignments as describe earlier are accentuated. To modify the data such that each angle is weighted approximately equally two things are done. First the log of the raw data $D_r(\theta)$ is taken (see figure 2.3). Then the log of the calculated reflectivity of a bulk sample of the same material as the top of the multilayer $B_c(\theta)$ is subtracted.

$$D_m(\theta) = \log[D_r(\theta)] - \log[B_c(\theta)] = \log \left[\frac{D_r(\theta)}{B_c(\theta)} \right] \quad (2.5)$$

To be consistent, the calculated values $C(\theta, d_1, d_2)$ are modified in the same way.

$$C_m(\theta, d_1, d_2) = \log[C(\theta, d_1, d_2)] - \log[B_c(\theta)] = \log \left[\frac{C(\theta, d_1, d_2)}{B_c(\theta)} \right] \quad (2.6)$$

An example of the raw data is in figure 2.1 and the same data after modification

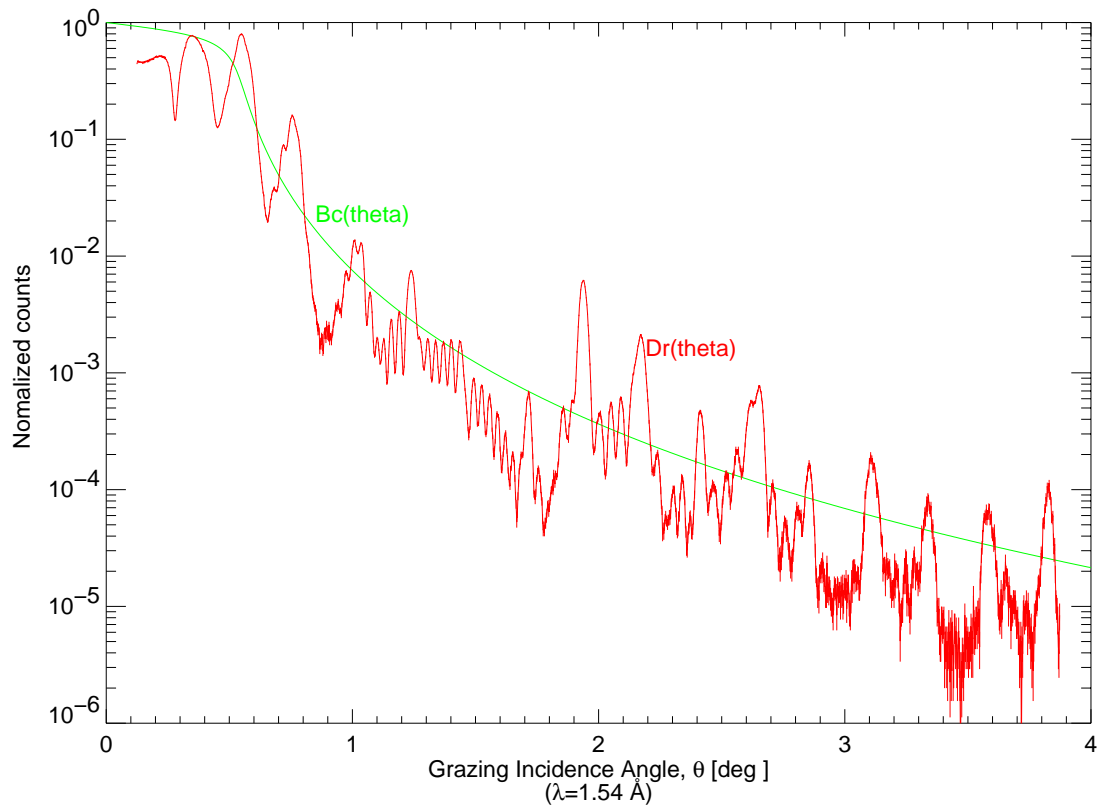


Figure 2.3: Comparison of reflection off a multilayer, Dr , and reflection off a bulk sample, Bc .

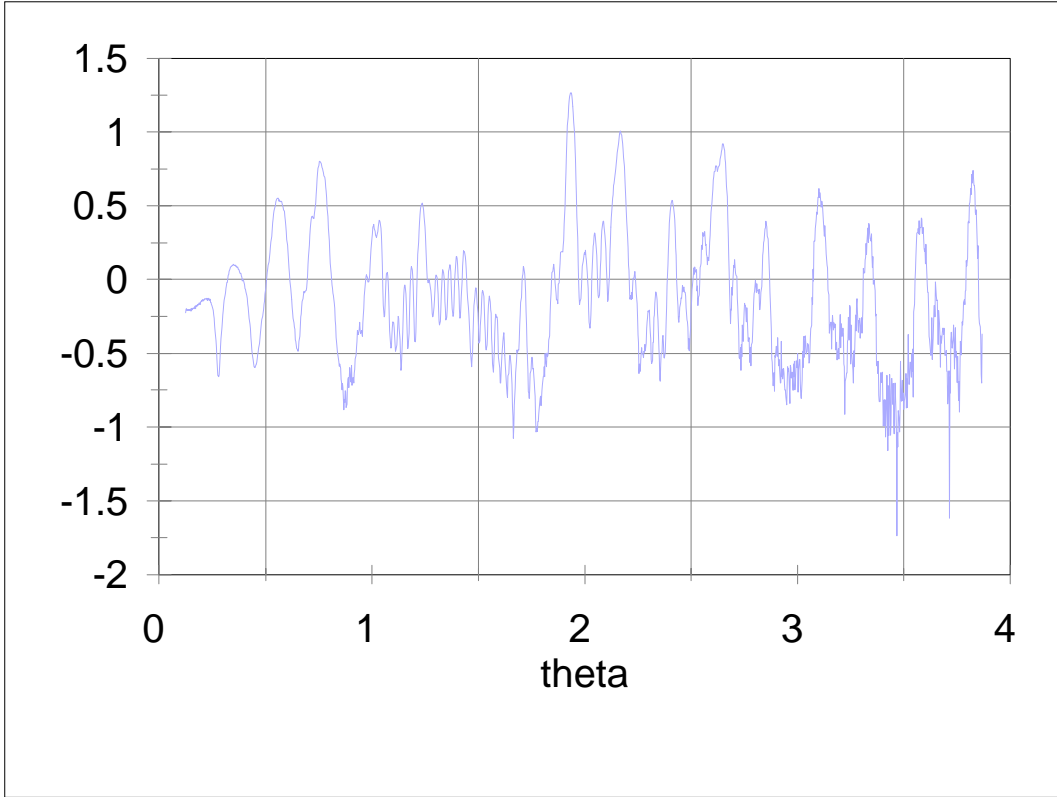


Figure 2.4: Modified XRD Data.

is in figure 2.4. The data at higher angles is less accurate because reflections there are so small. Modifying the data in a way that would reflect this would likely be better. There may also be other ways to modify the data such that variations in the fit parameters are accentuated. Further research into how the data could be modified could greatly improve the usefulness of XRD data.

To compare the two modified data sets $D_m(\theta)$ and $C_m(\theta, d_1, d_2)$ the Pearson's correlation coefficient P_c is used. This value has two advantages over simple least squares. First, it is independent of normalization - it only depends on the relative shape of the two data sets. Second, the value it gives is more meaningful. The

value is always less than 1 and greater than -1. This allows the goodness of a fit to be quantified. The Pearson's correlation coefficient is simply the normalized inner product of the deviance of the data from its mean. If each data set is thought of as a multi-dimensional vector with each θ value being a new dimension then P_c is the cosine of the angle between the two vectors. So if the value of P_c is close to 1 then the two data sets line up, i.e. they are a good fit. If P_c is equal to 0 then they are going in perpendicular directions and it is a bad fit. If the value is negative then they are going in opposite directions.

To calculate P_c first the average over θ is calculated for both data sets.

$$\overline{D_m} = \frac{\sum_{\theta} D_m(\theta)}{N} \quad (2.7)$$

$$\overline{C_m(d_1, d_2)} = \frac{\sum_{\theta} C_m(\theta, d_1, d_2)}{N}, \quad (2.8)$$

where N is the number of θ values. These average values are then subtracted from each point in their respective data sets.

$$D_m(\theta) - \overline{D_m} \quad (2.9)$$

$$C_m(\theta, d_1, d_2) - \overline{C_m(d_1, d_2)} \quad (2.10)$$

The value of each set at each point is then multiplied by each other and summed over θ . All this is then normalized by dividing by the standard deviation of each data set and by $(N - 1)$, the total degrees of freedom.

$$P_c(d_1, d_2) = \frac{\sum_{\theta} [D_m(\theta) - \overline{D_m}] [C_m(\theta, d_1, d_2) - \overline{C_m(d_1, d_2)}]}{s_{DSC}(N - 1)} \quad (2.11)$$

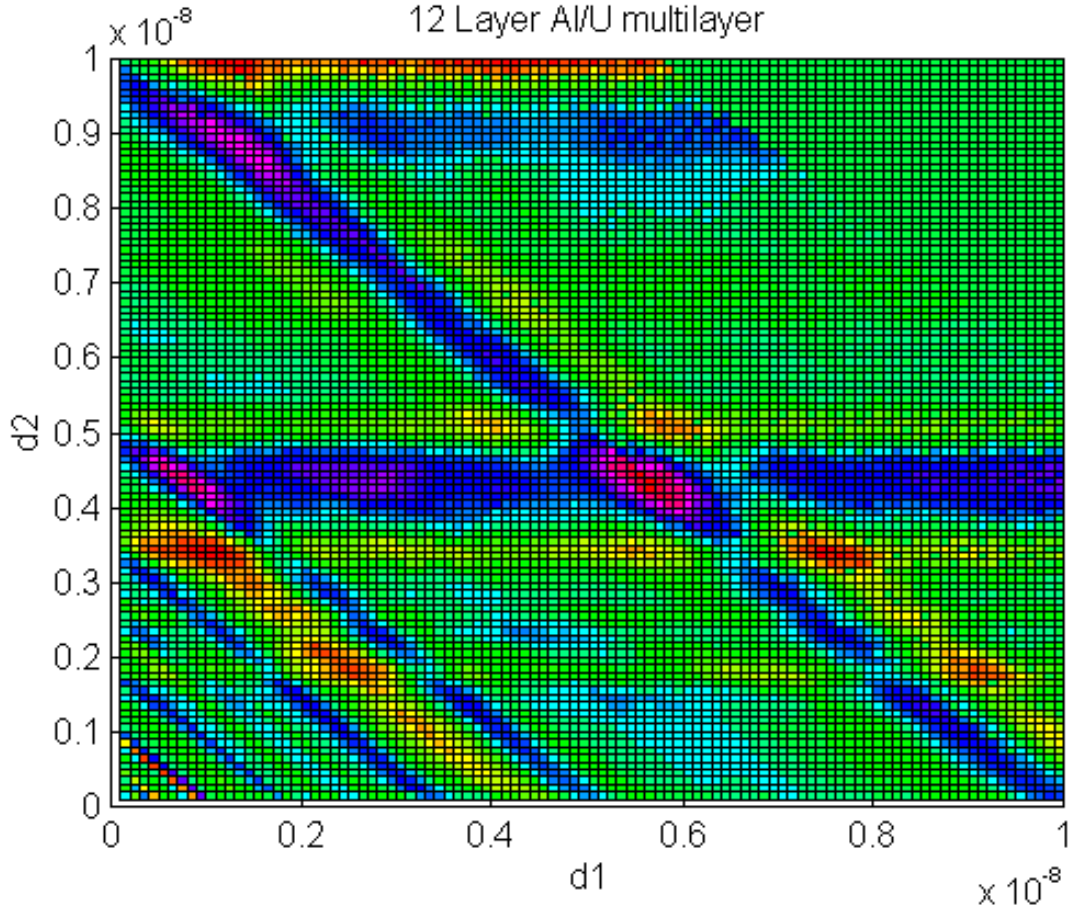


Figure 2.5: d_1 and d_2 space for a uranium/aluminum multilayer.

where

$$s_D = \sqrt{\frac{\sum_{\theta} [D_m(\theta) - \overline{D_m}]^2}{N - 1}} \quad (2.12)$$

and

$$s_C = \sqrt{\frac{\sum_{\theta} [C_m(\theta, d_1, d_2) - \overline{C_m(d_1, d_2)}]^2}{N - 1}} \quad (2.13)$$

The best fit is a maximum of $P_c(d_1, d_2)$. A plot of the $P_c(d_1, d_2)$ space for a uranium/aluminum multilayer is shown in figure 2.5. It is visually easy to find the

maximum of this plot. Where the straight horizontal line intersects with the diagonal line is the maximum. The correct value of d_1 and d_2 are the x and y coordinates at the center of the point where these two lines intersect. The other features within the plot could give additional information about the multilayer. In general the diagonal lines represent d-spacing. The horizontal or vertical lines represent thicknesses of individual layers within a period. The other diagonal lines in the lower left hand corner of figure 2.5 could just be ‘harmonics’ of the primary d-spacing line and not have a physical interpretation. To help interpret what is physical and what is not, XRD data was generated from a hypothetical multilayer and ran through the same process as the real XRD data. A $P_c(d_1, d_2)$ surface plot of two of these hypothetical data sets are shown in the appendix in figure A.1 and A.2. These also have additional lines at a lower d-spacing. Further research needs to be conducted to determine just what can be learned from these types of plots.

2.2 Ellipsometry

2.2.1 Ellipsometry Theory

Ellipsometry uses the fact that materials reflect s and p polarizations differently. It measures a ratio of the reflectance of the two polarizations by measuring ψ and Δ as defined in equation 2.14.

$$\frac{R_p}{R_s} = \tan(\psi)e^{i\Delta} \quad (2.14)$$

Where R_p and R_s are the complex ratios of the reflected electric field to the incident electric field for the different polarizations (see section 1.3). An advantage of ellipsometry over other reflectance measurements is that ellipsometry is able to measure the phase Δ . Other reflectance measurements simply measure the intensity of the reflected beam. This additional phase information makes this technique more sensitive to parameters in the optical system being measured.

2.2.2 Experimental Setup

A variable angle spectroscopic ellipsometer made by J. A. Woollam was used to collect data from the samples. It can measure ψ and Δ at 44 different wavelengths from 2861 Å to 6052 Å. It is also configured with a manual stage goniometer. Ellipsometric measurements can practically be taken from about 5° to 85° from normal.

Analysis of the data was done with software that came with the ellipsometer. This software allows the user to specify a model for a data set and then fit any parameters of that model to the data. It allows up to ten different model - data set pairs at the same time, and has the ability to couple any of the parameters of one of these ten models to any of the other ones. In this way it is possible to use more than one data set to find a given parameter. For example, if the user had two samples of the same unknown thickness, then the thickness in the model for each data set could be coupled to each other. This makes it so the two thickness are not allowed to vary independently in the fit algorithm. In this way the data from both samples are used to determine the thickness.

The software uses a method called the Levenberg-Marquardt algorithm to find the minimum in the parameter space. This method is a hybrid of the gradient method and the inverse Hessian method. The gradient method first determines the direction of the steepest slope and takes a step in that direction. The inverse Hessian method fits an N dimensional parabola to the surface then jumps to the minimum of that parabola. The Levenberg-Marquardt algorithm shifts from the gradient method when far from a minimum to the inverse Hessian method when close to a minimum. The value that it minimizes is the mean-squared error (MSE), and is defined as

$$MSE = \frac{1}{2N - M} \sum_{i=1}^N \left[\left(\frac{\psi_i^{\text{mod}} - \psi_i^{\text{exp}}}{\sigma_{\psi,i}^{\text{exp}}} \right)^2 + \left(\frac{\Delta_i^{\text{mod}} - \Delta_i^{\text{exp}}}{\sigma_{\Delta,i}^{\text{exp}}} \right)^2 \right] \quad (2.15)$$

This is similar to χ^2 but is normalized by dividing by $2N - M$ where N is the number of ψ, Δ pairs and M is the number of fit parameters. [15]

2.3 Transmission Electron Microscopy

2.3.1 TEM Theory

Transmission electron microscopy involves observing electrons that are transmitted through a sample from an incident electron beam. The electrons are emitted from a source such as a tungsten filament that is heated to a temperature just below its melting point. The electrons emitted from the filament are accelerated through a voltage potential and channeled into a small beam with electromagnetic lenses. This beam then interacts with the sample. Depending on the makeup of the sample the electrons are either transmitted through the sample or scattered. To produce a light

field image the beam of electrons that are not scattered continue down the column and pass through a number of other magnifying electro-magnetic lenses. The beam is then incident on a phosphor screen, film, CCD or other imaging device. In this way an image of how the electrons interact with the sample is generated. [16]

Because silicon is a low density semiconductor with a relatively small atomic number and uranium is a relatively dense metal with high atomic number there is a great deal of difference in the way they scatter electrons. This makes imaging uranium/silicon multilayers with TEM relatively easy. The hardest part is sample preparation. Getting a sample thin enough to allow electrons to transmit through it, without destroying the part of the sample that is of interest, can be a real challenge. A common procedure uses ion milling. However this procedure can be very time consuming. In addition, the success rate for this procedure is not that good, especially for a less experience microscopist. A simpler technique with a better success rate is the small angle cleavage technique.

2.3.2 Small Angle Cleavage Technique

Small angle cleavage technique is a promising technique for preparing thin films for TEM analysis. It causes less sample damage to the sample than ion milling and uses more common equipment. It “uses only hand tools such as a scribe and tweezers and readily available laboratory equipment such as a sample grinder, a low-power stereo light microscope, a hot plate and a low temperature oven” [17]. Originally this technique was primarily used to look only at crystalline specimens and was primitive.

The following is a brief description of the technique by Goodhew published in 1972:

To prepare slices initially it is usually sufficient to strike the crystal sharply on its edge with a razor blade and then to select from the resultant debris suitably shaped pieces. A piece of tape is pressed on to a freshly macro-cleaved surface and then pulled off from one end, taking a flake of the material with it. This process is repeated until small enough flakes are clinging to one of the pieces of tape. [18]

Since then, more precise techniques have been developed. These techniques are designed for looking at thin films on crystalline substrates. Walck and McCaffrey [19] give detailed step-by-step directions, with photos, on how to use this technique for thin films. They include alternative methods for different materials and a large section on things to consider and “tips and tricks.” A summary of the procedure is as follows:

1. A small (approximately $2\text{mm} \times 3\text{mm}$) sample is scribed and broken from the wafer. All but a thin layer ($100\ \mu\text{m}$) of the substrate is removed by grinding. This is done on a polishing wheel with 15 to $30\ \mu\text{m}$ abrasive paper. When the sample gets close to the desired thickness care is taken to make the scratch marks from the abrasive paper between $12 - 15^\circ$ from the long side of the sample.
2. A diamond scribe is used to score lines every 0.5 mm in the same direction as the scratch marks from the polishing. The sample is then removed from the polishing mount and carefully broken along the scribe lines.

3. There should be five or six pieces to work with. These pieces are turned over, so that the side with the thin film is up. A small scribe line is made sideways along a corner of the sample. This is done with a mini-diamond scribe under a microscope. As the scribe line is made, light pressure is applied so that a fracture will propagate slowly to the edge of the sample. This should produce a very small, very sharp wedge shaped piece of the sample. This process is repeated for all of the five or six pieces.

4. The thin edge of each wedge shaped piece is examined under a powerful light microscope. If the edge cannot be seen, it is probably thin enough for the transmission electron microscope, otherwise it is discarded. One or more of the good pieces are mounted on a single hole grid (see figure 2.6). The grid is placed in the microscope for examination.

This technique is relatively easy to learn, but parts of it take practice to do well. I found that the most difficult part was the final scribing (part 3). It is absolutely necessary to use a mini-diamond scribe for this step. A standard-sized scribe is much too difficult to work with under the microscope. A big advantage of this technique is that there are many pieces to work with. Because of this there are typically about twelve chances to get the last two steps correct.

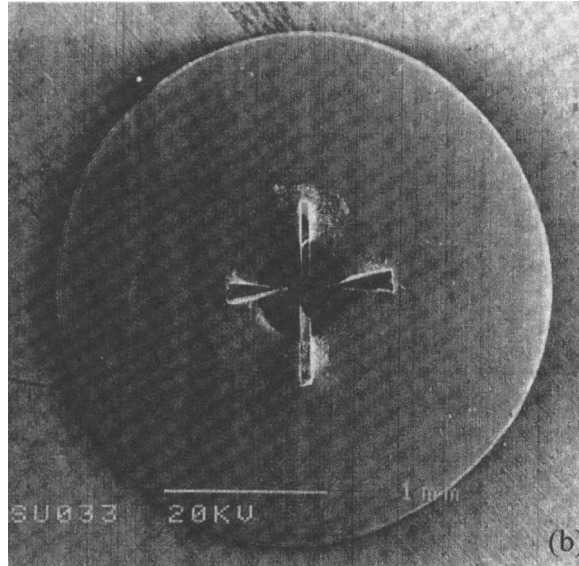


Figure 2.6: Four wedge-shaped samples mounted on a single hole TEM grid[17].

2.4 X Ray Photoelectron Spectroscopy

X ray photoelectron spectroscopy (XPS) is a powerful surface analytical technique. Combined with sputtering it can give a wealth of information concerning the composition of a thin film. It cannot only tell what elements are in a specimen but can also indicate how those elements are bonded. XPS cannot give an exact composition versus depth profile because different materials have different sputter rates. However, with careful analysis it can give a good indication of composition versus depth.

The XPS process involves irradiating a sample with X rays and observing the energy of the electrons that are emitted. The X rays are typically either Al $K\alpha$ (8.29 Å, 1486.6 eV) or Mg $K\alpha$ (9.83 Å, 1253.6 eV). When these X rays interact with the electrons in an atom, electrons bound with less energy can be removed as described

by the photoelectric effect. The ejected electrons' kinetic energy is the difference between the photon's energy and their binding energy. The energy of these electrons is then measured and referenced to the energy of the original X ray. Analysis of the energy lost versus counts of electrons reveals characteristic peaks for the electrons of different elements.[20]

Figure 2.7 shows two peaks for uranium in the 385 eV region from the $4f_{5/2}$ and $4f_{7/2}$ electrons and two others in the 100 eV region from the $5d_{5/2}$ and $5d_{3/2}$ electrons. The large peak at 530 eV is from the oxygen 1s electron. Much smaller peaks for carbon at 285 eV and Si at 150 eV can also be seen [21]. By looking at the relative intensities of the peaks for different elements and by knowing sensitivity factors for each peak one can get a percent composition for each element. Careful analysis of any shifts in characteristic peaks can also lead to binding information.

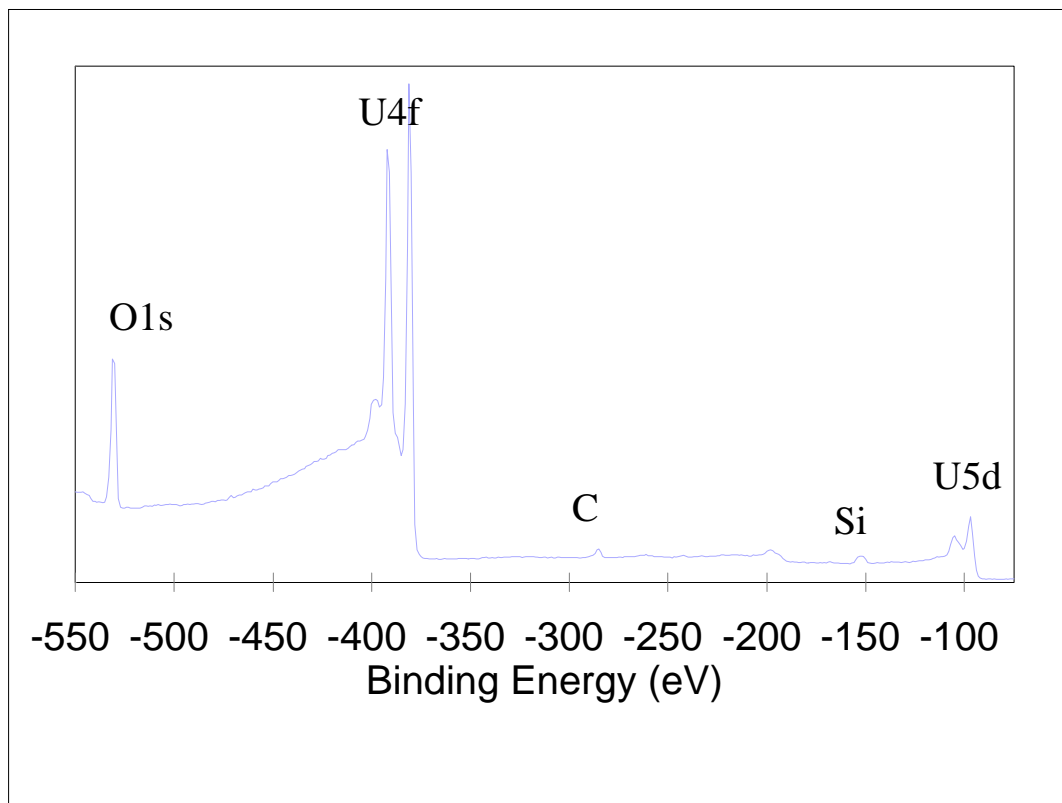


Figure 2.7: XPS scan of U8Si157.

Chapter 3

Results

The methods described in the previous chapter along with atomic force microscopy were used to characterize six samples. One of the samples is a uranium/silicon multilayer (U8Si157) that was made as a practice run for the IMAGE mission mirrors. The others are all single layers of uranium (U66, U67, U68, U69, U70). All of the samples were allowed to oxidize in air. Parts of some of these samples were also annealed at 90°C (U67B90,U68B90) and other parts at 180°C (U67B180,U68B180). The “B” after the sample name indicates that it was annealed. The number after the “B” refers to the approximate annealing temperature. The number before the “B” and after the “U” were assigned sequentially as samples were made, arbitrarily starting with the number 66. This chapter gives data collected from these samples and provides interpretation of that data when possible.

3.1 Depth Profile

3.1.1 Atomic Force Microscopy

The roughness of two different samples was measured with atomic force microscopy (AFM). The first, U66, is a single layer of uranium oxide. The uranium layer was deposited in August of 1999. Using the sputter rate of uranium determined by X ray diffraction the original pure uranium thickness of this sample is about $50 \text{ \AA} \pm 4\%$. It was allowed to oxidize at room temperature for over nine months. After it had oxidized the thickness, also measured by X ray diffraction, was about $110 \text{ \AA} \pm 2\%$. The second sample, U68B180, is also a single layer of uranium oxide, but it was deposited in May of 2000 and then annealed in air for more than a day at about 180°C . Its estimated original thickness is about $150 \text{ \AA} \pm 4\%$. After it had oxidized it was determined with X ray diffraction to be about $400 \text{ \AA} \pm 2\%$ thick.

As expected the annealed sample is the rougher of the two. It was measured with AFM to be 4.4 \AA rms roughness over a $1 \mu\text{m}$ area. The room temperature sample has about 1.4 \AA rms roughness. It is difficult to tell just how much of this roughness can be attributed to noise and instrument error. Most of the features seen in the AFM scan for U68B180, the annealed sample, (figure 3.2) did not change as the needle rastered back over them. So it is assumed that they are physical. This was not the case with most of the smaller features in the scan of U66 (figure 3.1). The accuracy of the calibration for height of the AFM at the 1 nm level and below is also questionable. So the roughness values should be considered approximate.

Roughness Analysis

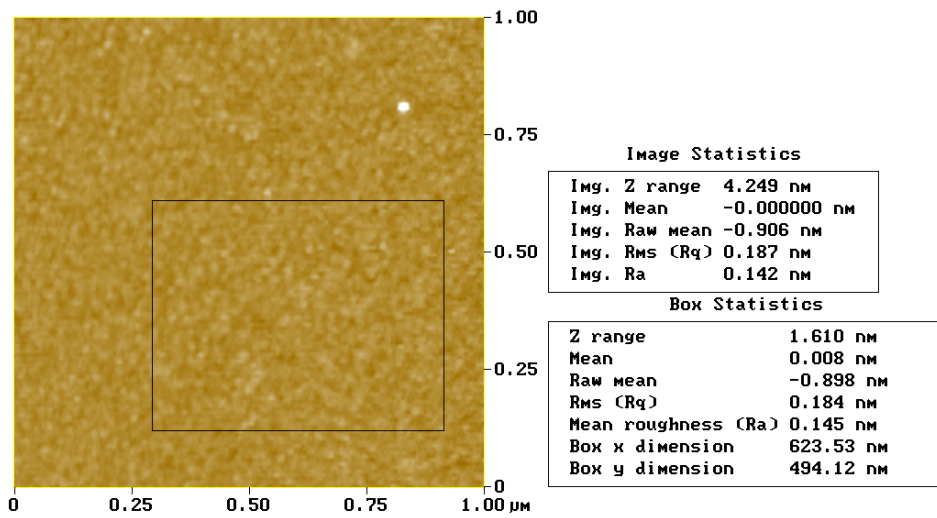


Figure 3.1: AFM surface image and analysis for U66. Lighter areas are higher parts, dark areas are lower.

Roughness Analysis

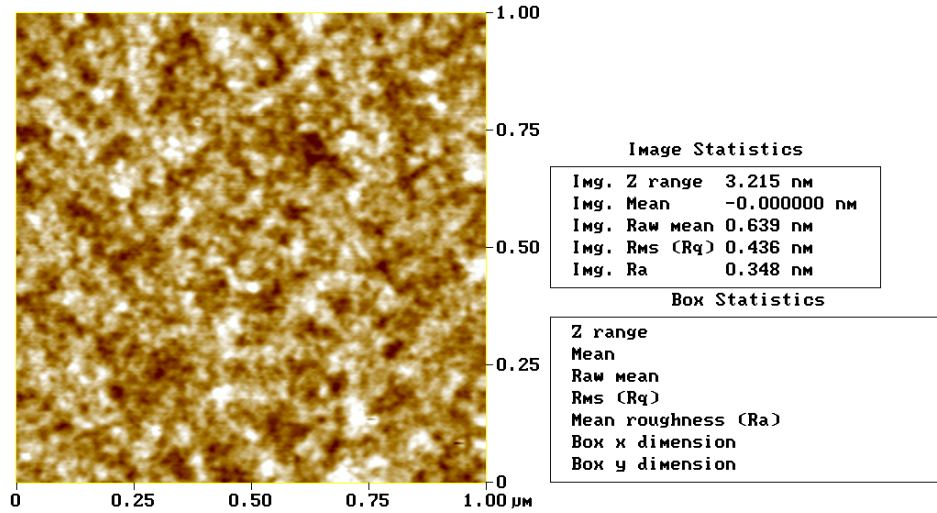


Figure 3.2: AFM surface image and analysis for U68B180. Lighter areas are higher parts, dark areas are lower.

3.1.2 X Ray Diffraction

X ray diffraction (XRD) was used to measure the thickness characteristics of many samples. Primarily, it was used to measure thicknesses of single layers of uranium oxide, but it was also used to characterize the uranium silicon multilayer U8Si157. To find the thickness of the single layers the old method of visually comparing data with calculated values as described in section 2.1.3 was used. This was used because with a single layer it is relatively easy and fast to do, and because the other method (section 2.1.3) had not been completely developed. The new fitting method was used to fit the XRD data for the uranium-silicon multilayer U8Si157. Optical constants for uranium at 1.54 \AA were obtained from CXRO's web site [22]. The index of

Table 3.1: Summary of XRD Measurements of Single Layer Uranium Samples.

Sample Name	Thickness in Å			
	Sputtered	Room Temp	Annealed 90°	Annealed 180°
U66	50 ±2	105 ± 2		
U67	200 ±8	385 ± 3	470 ± 10	475 ± 10
U68	150 ±6	310 ± 5	396 ± 2	404 ± 2
U69	100 ±4	265 ± 5		
U70	400 ±16	645 ± 5		

refraction obtained for uranium with a density of 18.92 grams/cm³ on this site is $n=(1 - 4.47131 \times 10^{-5}) - i(7.29783 \times 10^{-6})$.

There were five different single layer uranium samples made: U66, U67, U68, U69, U20. Parts of some of these samples were annealed at about 90° C and other parts at about 180° C. The thickness values that were measured with XRD are summarized in Table 3.1. The difference in optical constants at this energy between uranium and uranium oxide is not large enough for XRD measurements to tell the difference. So the thicknesses shown should be considered as the sum of the oxide thickness and the thickness of any non-oxidized uranium layer, if any. The uncertainty range is based on a subjective analysis of the quality of the visual fit.

To characterize the uranium-silicon multilayer, U8Si157, a graph of the d and Γ space was studied. The strong line that extends over all possible gammas in figure

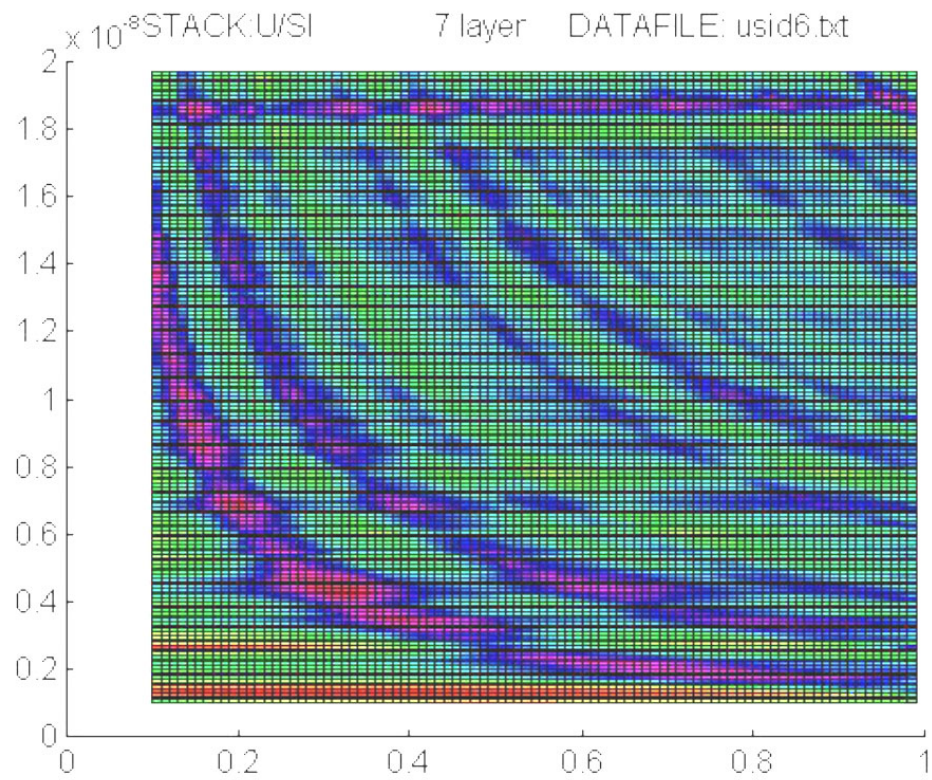


Figure 3.3: d and Γ space for U8Si157. Dark horizontal line near the top represents a d -spacing of 187 \AA , other curved lines represent possible Γ values.

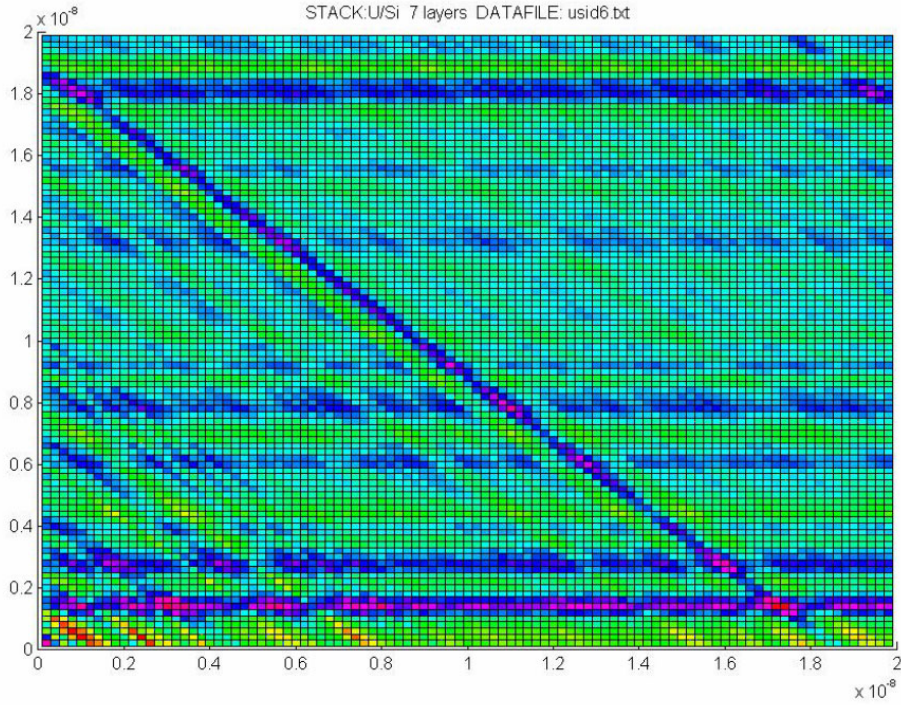


Figure 3.4: d_1 and d_2 space for U8Si157.

3.3 indicates that the correct d spacing for this sample is 187.0 Å. A plot of the d_1 uranium, d_2 silicon space (figure 3.4) makes it easier to interpret other features in the plot. Although not all these lines represent physical thicknesses, some of them do. There are two horizontal lines that represent the thicknesses of the d_1 and d_2 at 56 Å and 131 Å respectively. There is also a relatively strong line at about 30 Å. This line could represent the thickness of the uranium oxide cap. It is not yet clear how much information can be extracted from a plot like this, but the line near 30 Å is at least supporting evidence of the thickness of the top uranium oxide cap.



Figure 3.5: TEM image of U8Si157.

3.1.3 Transmission Electron Microscopy

Sample U8Si157 was also analyzed by transmission electron microscopy (TEM). There were many images taken but the most revealing is shown in figure 3.5. The 187 \AA d spacing is confirmed by comparing the period in the image to the scale. Also with careful analysis the thin top layer of uranium looks like it is between 25 and 35 \AA thick. This image can also give information about diffusion. The small angle cleavage technique (section 2.3.2) produces a sample that has a wedge shape. The image is taken by looking at the thinnest edge of the wedge. The orientation of the sample is such that it is thicker on the right side of the image in figure 3.5. Between the uranium, the thick dark lines, is the lighter silicon. However, all the lines get dark on the right side of the image because the sample is thicker there. The silicon lines stay lighter on the part that is further down the stack. This indicates that the uranium layer above it has diffused into the silicon clear down to the next uranium layer, and that the concentration of this diffused uranium decreases approximately linearly with the depth of the silicon layer.

3.1.4 X Ray Photoelectron Spectroscopy

X ray photoelectron spectra were compared to spectra published in an article by Teterin, *et. al* [23]. It gives a detailed study of changes in a number of the XPS peaks of uranium and oxygen for different oxides of uranium from UO_{2+x} with $x < 1$. This thesis uses for comparison the binding energy range from 0 to 40 eV which includes U5f, U6p, U6p1 and O2s peaks. It also uses the two peaks of uranium in the range

from 375 to 410 eV (U4f7 and U4f5) and oxygen 1s at 531 eV.

First, a study of only the surface of three samples was conducted. A very clear difference in the samples was observed in the doublet for uranium U4f7 and U4f5 (figure 3.6). The spectra that is different is from a sample (U67C) that was relatively fresh, about a month old, when it was measured. The two spectra that are the same are from the samples U67B180 and U8Si157. U67B180 is also a month old, but it was annealed at 180° C for about two days. Sample U8Si157 had been sitting in air for more than a year. It is not too surprising to see that the older sample is more like the annealed sample. Uranium oxidizes very quickly in air to UO_{2+x} (section 3.3). This data also shows that long time scales can also make a difference in the surface oxidation of uranium. The fresh sample spectra matches very well with the published spectra for UO_2 . The two peaks in the other spectra are shifted to higher binding energies. This indicates a higher oxide. They do not compare exactly but the closest match in the article is $\text{UO}_{2.13}$.

The spectra for O1s (figure 3.7) reveals more information about the surface of these samples. The peak for O1s is at a higher binding energy than that of U4f uranium doublet. This means that the electrons measured for it have less kinetic energy when they leave the atom. So they cannot travel as far through a material. This makes the O1s peak more subject to surface effects. All of the samples show components of two peaks. This indicates that all are a greater oxide than UO_2 . I would speculate that U67C has a thin layer of higher oxide, perhaps a monolayer or two, and that U67B180 is a higher oxide, perhaps $\text{UO}_{2.1}$, that is more uniform

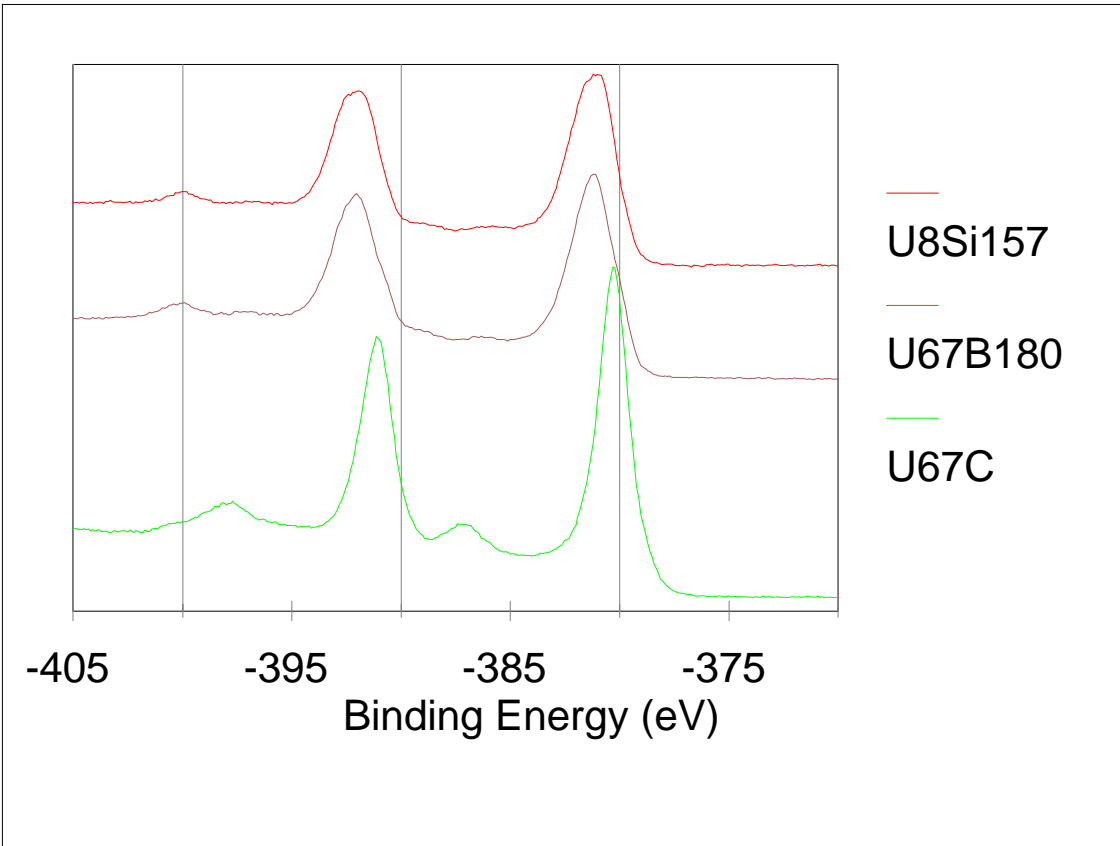


Figure 3.6: XPS data for 4f uranium doublet. Comparison of old (U8Si157), annealed (U67B180) and fresh (U67C) samples.

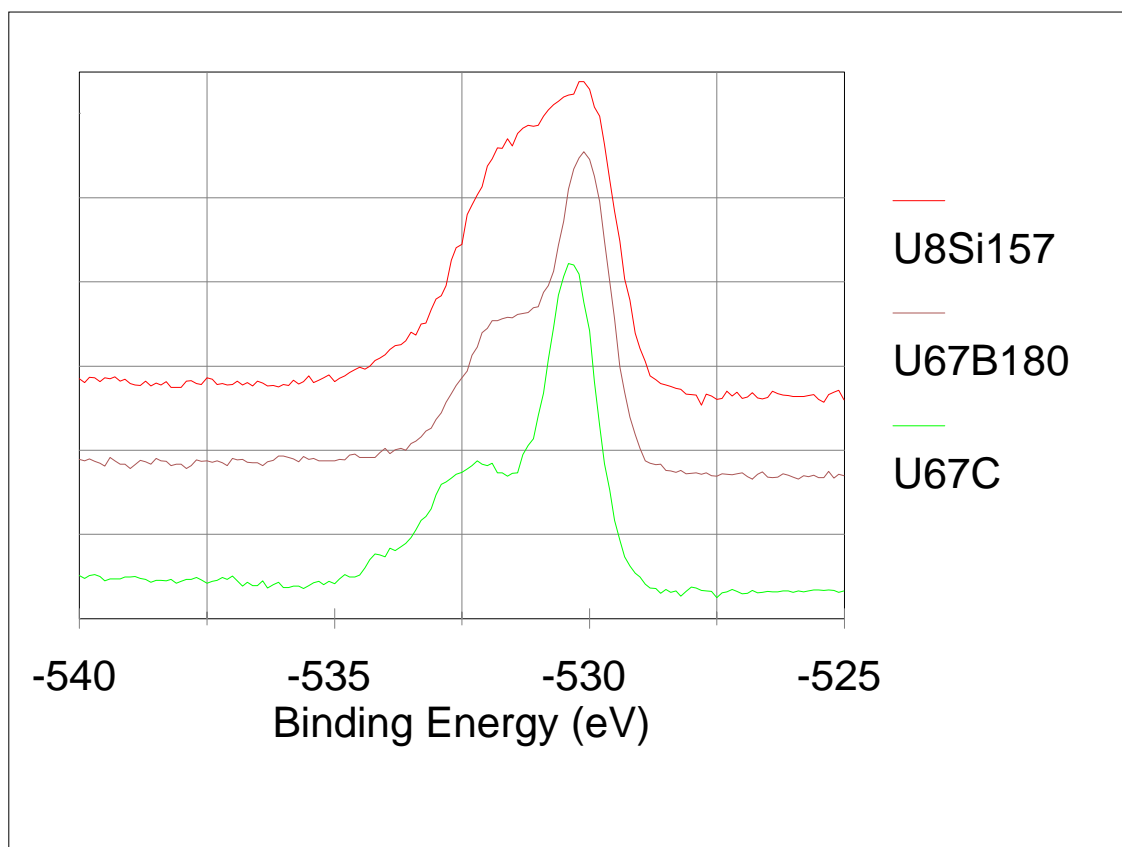


Figure 3.7: XPS data for oxygen 1s. Comparison of old (U8Si157), annealed (U67B180) and fresh (U67C) samples.

throughout the sample. The top of U8Si157 is likely to be similar to U67C but have a thicker layer of a higher oxide.

XPS was combined with sputtering multiple thin layers off the surface to produce a detailed composition versus depth profile for U8Si157. The sputter rates for a few common elements were listed in the documentation that came with the spectrometer, but uranium was not one of them. The slowest sputter rate listed was about 0.1 Å per second. There are many variables that can change the sputter rate. The type

of elements on the surface and how they are bonded as well as user-defined variables like the sputter spot size and the current all affect sputter rates. In addition, the technician running the spectrometer was still learning how to sputter at the time she sputtered our sample. With all these variables it is difficult to estimate the sputter rate without inferring it directly from the data. The data showing the peaks for Si2p and U5d5 and U5d3 (figure 3.10) indicates a shift from mostly uranium to mostly silicon somewhere between 430 to 1030 seconds of sputtering. Assuming the top uranium layer is between 25 and 35 Å, this gives a range of the sputter rate from 0.024 Å/s to 0.081 Å/s. These seem a little low, but considering the number of unknown variables they are still reasonable. For the remainder of this section, a sputter rate of 0.053 Å/s will be assumed.

There are a number of transitions that are noticeable in the sputter XPS data for the multilayer U8Si157. The first happens within the first 30 seconds of sputtering. This corresponds to about 1.6 Å, but XPS only has a depth resolution of about 10 to 20 Å depending on the material [25, 24]. So a better estimate of the depth for this transition would be between 5 and 15 Å. This transition is from a higher oxide, perhaps UO_{2.2}, to uranium dioxide and is indicated by a small shift in binding energy as seen in figure 3.8.

Another transition from 90 s to 190 s is noticeable by looking at the oxygen 1s peak (figure 3.9). This transition starts at about 5 Å and has a thickness of about 5 Å. The approximate 1 eV shift in binding energy of the O1s peak would signify a large change in the oxidation of uranium. However, the full width half max (FWHM) of

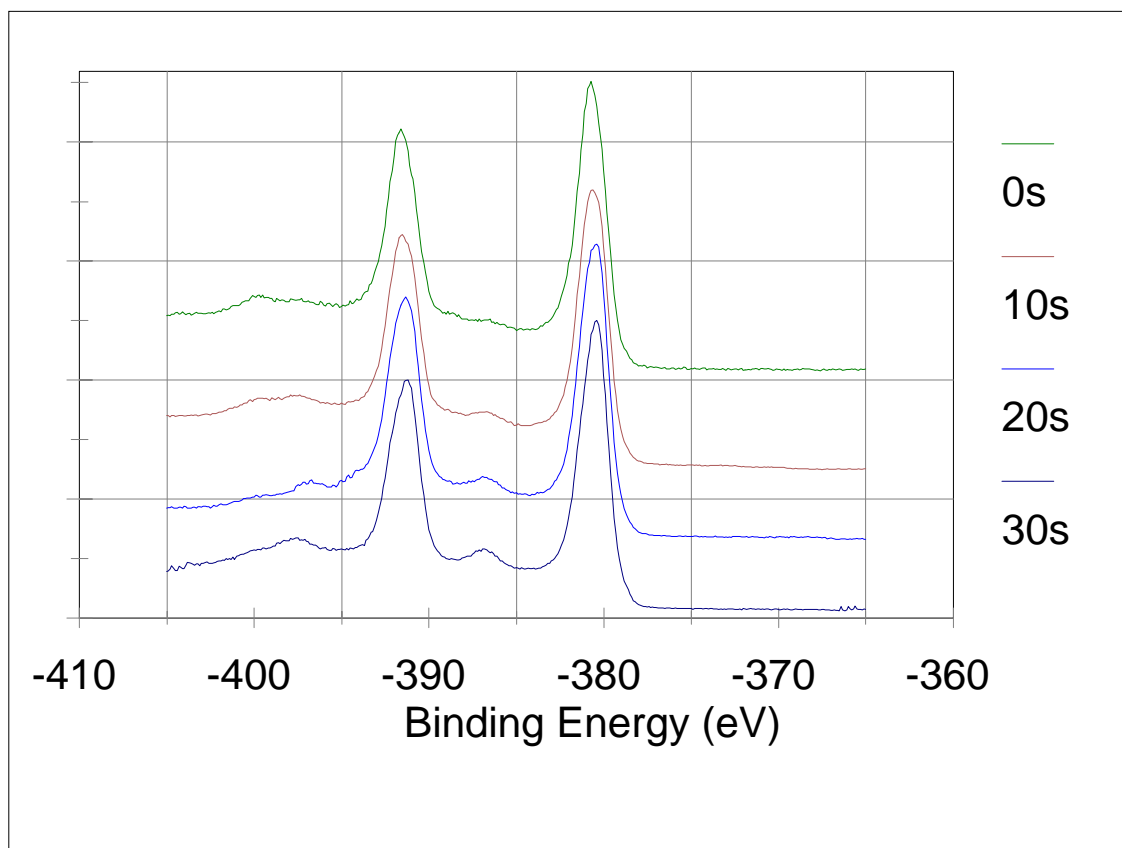


Figure 3.8: XPS depth profile data for U4f doublet. Time represents sputter time for removing surface layers and corresponds to depth.

this peak as a function of depth compared to the data given in reference [23] indicates otherwise. The FWHM of the peaks before the transition is 1.6 eV, exactly in line with the value given in the article for UO_2 . The FWHM for the peaks after the transition is 1.9 eV, where the FWHM given for $\text{UO}_{2.06}$ is 2.3 eV and for $\text{UO}_{2.13}$ is 3.0 eV. In addition, there is a shift of about 0.9 eV in the uranium 4f doublet, but there is no change in the relative position of the doublet and their satellites. This transition could simply be due to a small degree of charging. However, it is more likely due to a real transition of either a very small shift to a higher uranium oxide or more likely due to hydration or absorbed oxygen.

The next transition is the beginning of the boundary between the uranium oxide cap and the underlying silicon layer (figure 3.10). It happens between 430 s and 1030 s and can best be seen by looking at the Si2p peak at 100.1 eV. It is flanked on either side by the uranium 5d3 and 5d5 peaks. This makes it easy to compare the two intensities. As the uranium peaks decrease the silicon increases. The time of this transition corresponds to about 32 Å.

The last transition observed with this XPS data begins just after the previous transition starts (figure 3.11). It goes from 670 s (55 Å) to 1630 s (86 Å). This is the change from uranium dioxide to non-oxidized uranium. It is most easily seen by looking at the strongest of the uranium peaks, the uranium doublet 4f7 and 4f5 near 377 eV and 388 eV respectively. The two peaks in the beginning of the transition at 392 eV and 381 eV with the satellite peaks at higher energies are characteristic of uranium dioxide. The two peaks in the end of the transition at 377 eV and 388 eV

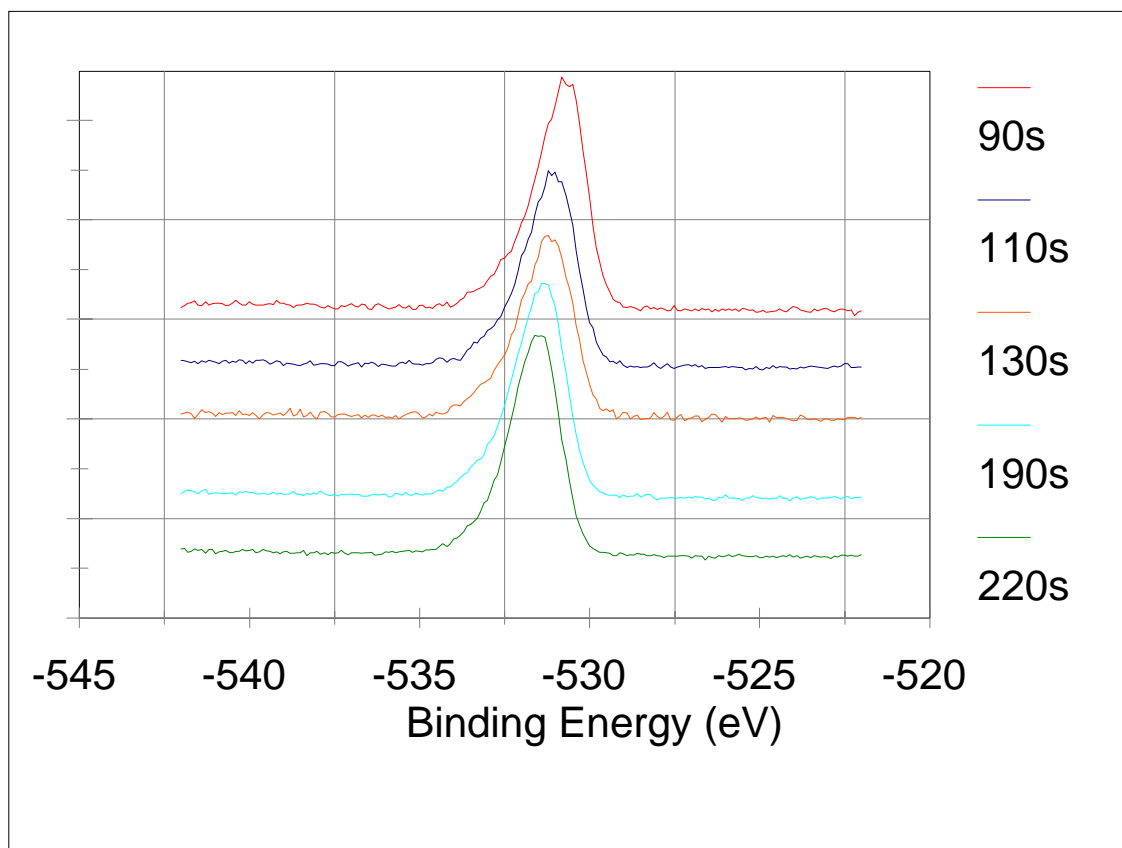


Figure 3.9: XPS depth profile data for oxygen 1s. Time represents sputter time for removing surface layers and corresponds to depth.

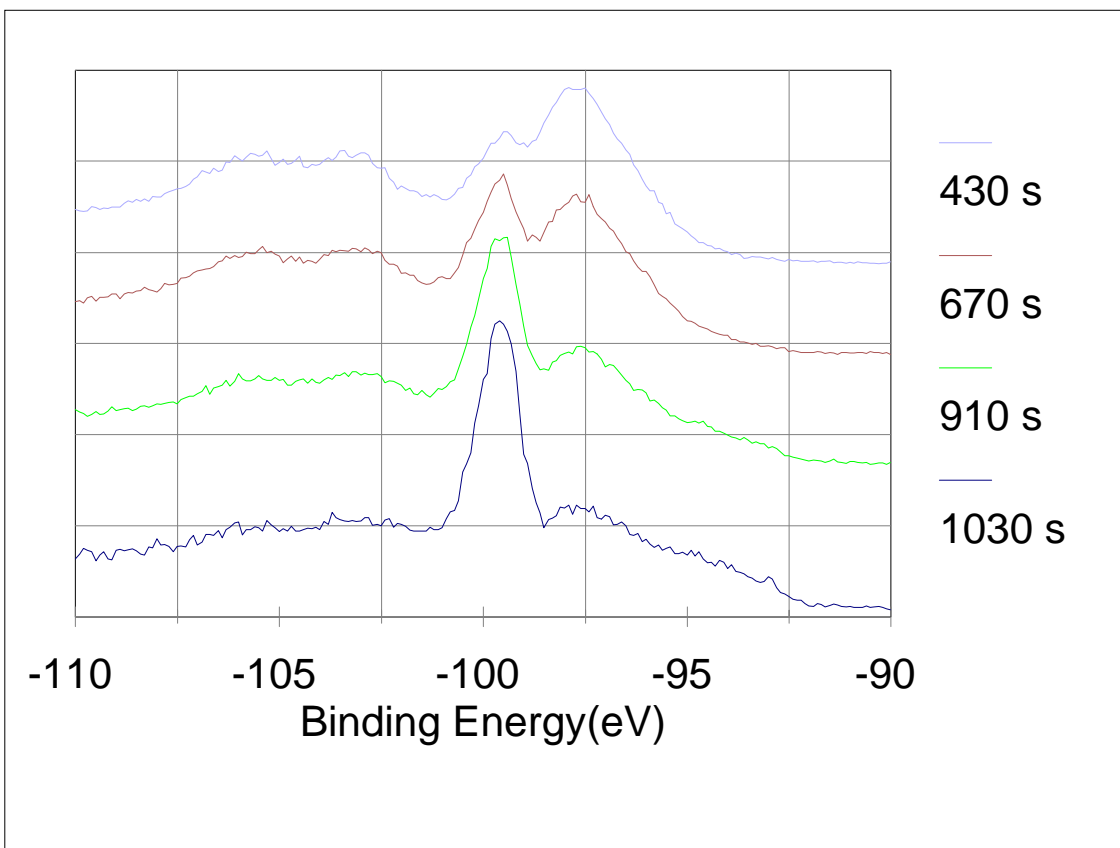


Figure 3.10: Transition from uranium to silicon. XPS depth profile data for U5d3, Si2p, U5d5. Silicon peak is in the center at about 100 eV. The two uranium peaks are on either side of the silicon peak. Time represents sputter time for removing surface layers and corresponds to depth.

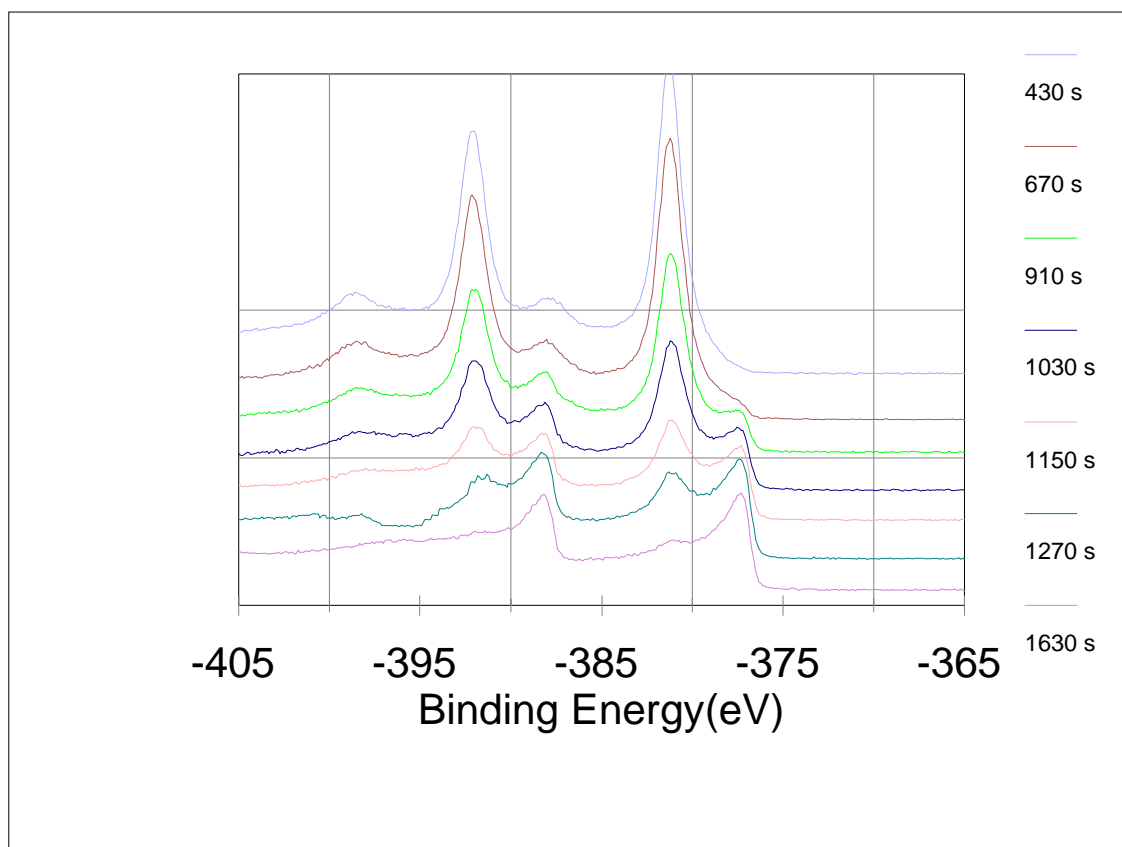


Figure 3.11: Transition from uranium oxide to uranium. XPS depth profile data for U4f doublet. Time represents sputter time for removing surface layers and corresponds to depth.

are characteristic of non-oxidized uranium.

It is significant that the transition from the oxide to non-oxidized uranium begins just after the silicon begins to dominate. The uranium oxide is still present some time after the silicon is introduced. For this reason I do not believe that the silicon itself prevents the oxide from forming. However, it appears that the silicon mixed with the uranium dioxide may inhibit the mechanism for further oxide growth of both

the uranium and the silicon. Further research is needed to explain exactly why the oxide growth did not continue further down the multilayer. A summary of all the transitions is shown in figure 3.12. The depths shown are approximated from the sputter rates as described previously. The stoichiometry of the top layer of uranium oxide is assumed as well as the shown hydroxide.

3.2 Optical Constants

To determine thicknesses for an oxidation rate study (section 3.3) optical constants in the visible and IR were needed for uranium and uranium oxide. The needed uranium optical constants were taken from published literature [26]. There have been a number of different studies on the optical properties of uranium dioxide [28, 29, 27]. However, the optical constants for uranium oxide can vary greatly depending on the value of x in UO_{2+x} [30, 31]. In addition, the role that a hydroxide plays was unknown. For these reasons, optical constants were determined using ellipsometric measurements. A method similar to the one Herzinger [32] used to determine optical constants for silicon and silicon dioxide was employed. Multiple angle, spectroscopic ellipsometric measurements were made on five different single layer uranium samples. Measurements were taken at different times so that a total of ten different sets of data were obtained (see Table 3.2). All this data was then used to simultaneously find the values of the uranium and oxide thicknesses for each of the samples as well as the optical constants for the top layer of oxide. This was done with the software that came with the ellipsometer as described in section 2.2.2. With all the different

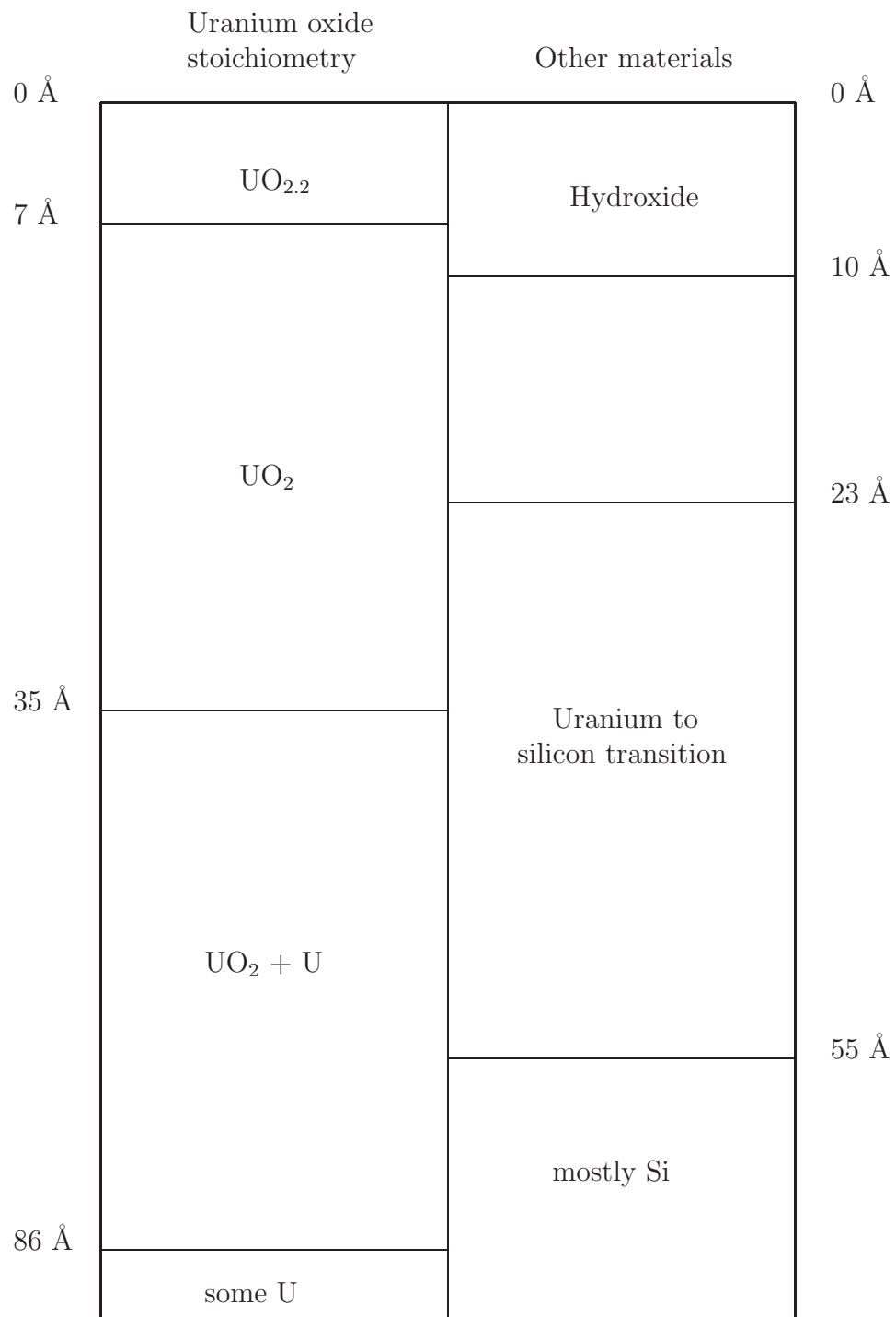


Figure 3.12: Hypothetical depth profile of uranium oxide cap on U8Si157.

angles, wavelengths and samples the total number of measurements used in the fit came to 5,368. The total number of parameters the software was finding with this data was 108. The MSE value (see section 2.2.2) was 7.6657. Generally an MSE value of less than 10 implies that the fit is good, i.e.. it has likely found a global minimum. The results of the real part of the index of refraction are shown in figure 3.13 and the imaginary part are shown in figure 3.14. As a comparison, both plots also show the index of refraction values published by Ackermann [27]. Differences in these values are likely due to measurement errors, the absorption of water vapor and/or slightly different stoichiometries. Transmission measurements of the oxide thin films would give additional valuable information about the index of refraction.

3.3 Oxidation Rates

3.3.1 Units

Most of the literature that discuss oxidation rates give rates in units of milligrams per centimeter squared per hour or per minute ($\text{mg}/\text{cm}^2/\text{h}$ or $\text{mg}/\text{cm}^2/\text{min}$). The measurements I took were thickness measurements. For this reason it is easier to discuss oxidation rates in units of angstroms per second ($\text{\AA}/\text{s}$). This section describes the relationship between these two sets of units.

First it is helpful to know the expansion ratio. This is the ratio of the thickness of the oxide (z') to the thickness of the amount of metal that oxidized to form the

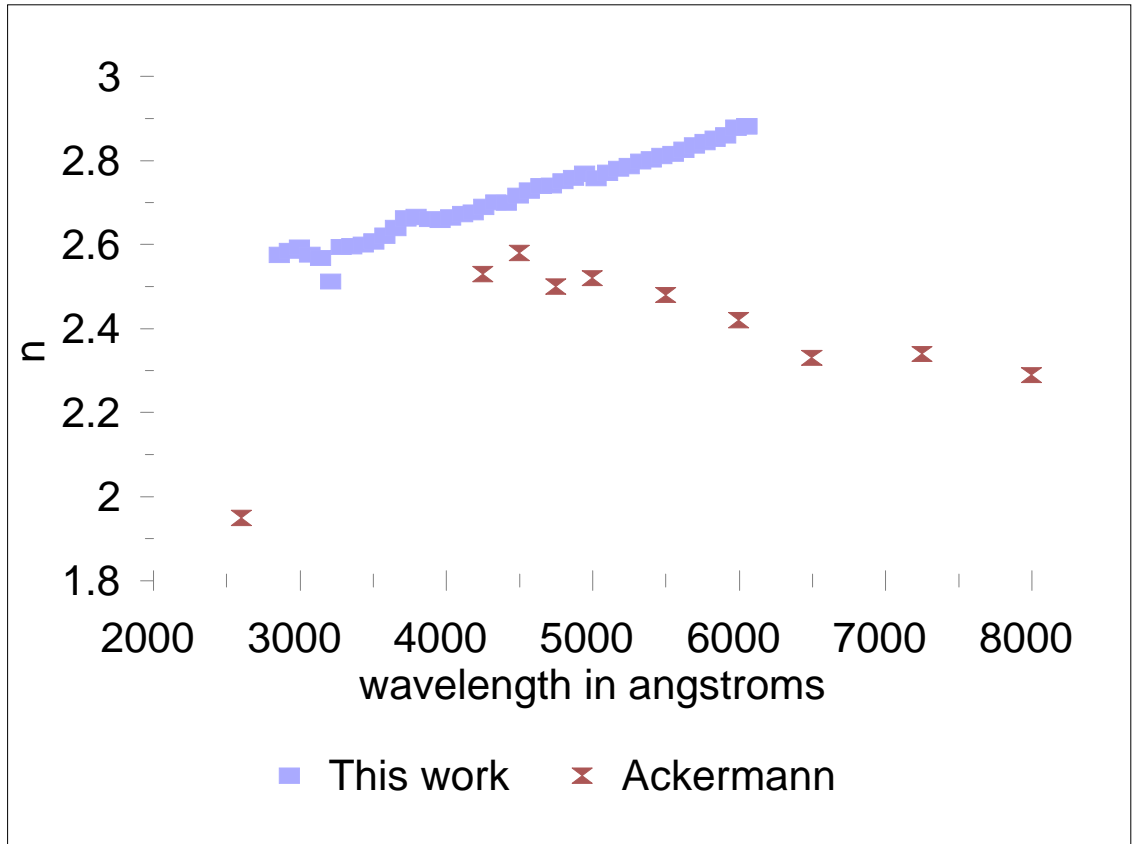


Figure 3.13: Real part of the index of refraction for uranium oxide. Comparison of values for uranium dioxide found by Ackermann to values determined in this study with ellipsometry.

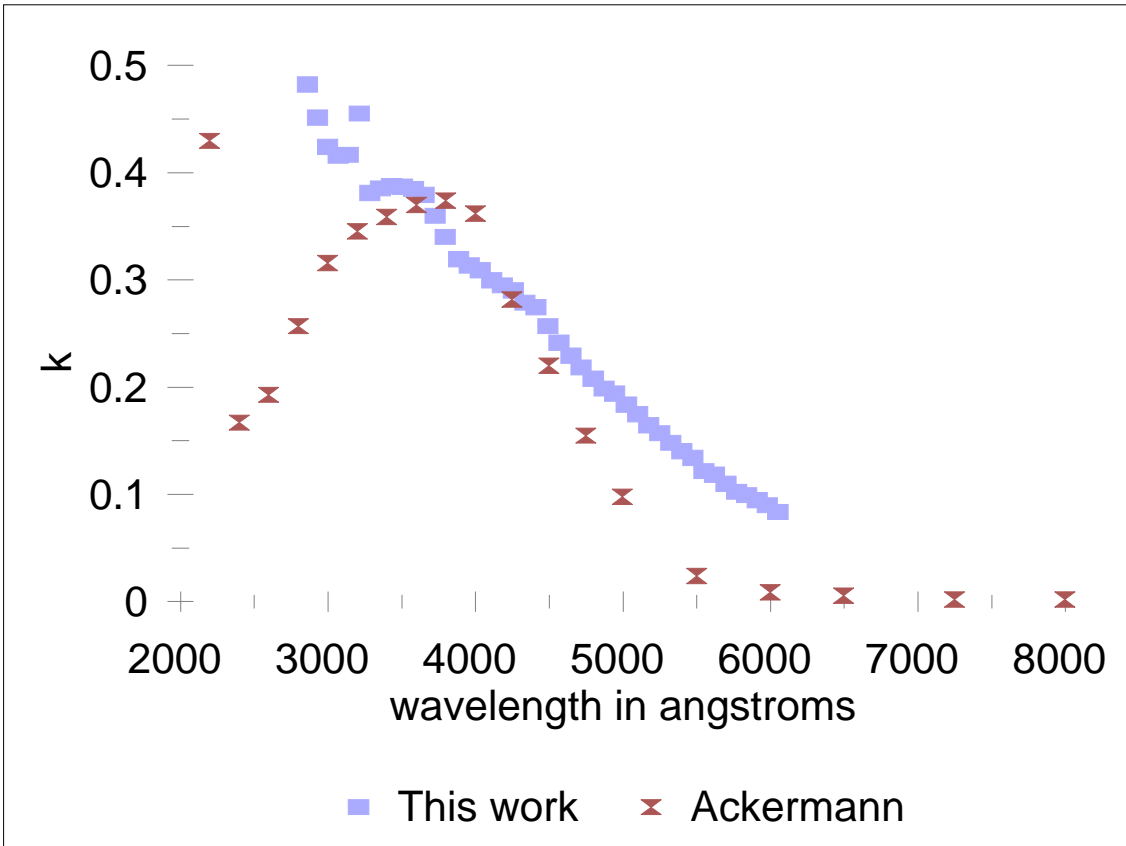


Figure 3.14: Imaginary part of the index of refraction for uranium oxide. Comparison of values for uranium dioxide found by Ackermann to values determined in this study with ellipsometry.

Table 3.2: Summary of ellipsometry measurements used for determining optical constants of uranium oxide, all thicknesses in Å. Time is time from removing from vacuum.

Sample	Time	Angles, step 5°	U thickness	Oxide thickness	Total
U66	10 months	40° to 80°	7.7±1.1	107.7±2.1	115.4
U67	16 days	45° to 85°	138.7±2.3	202.2±5.0	340.9
U67	26 days	45° to 80°	127.2±2.3	221.9±5.7	349.1
U68	1day	45° to 80°	132.6±1.6	130.4±2.8	263.0
U68	8 days	45° to 75°	96.7±1.9	187.8±4.6	284.5
U69	2hr 20min	50° to 80°	93.8±0.9	78.5±1.4	172.3
U69	5hr 4min	50° to 80°	71.1±1.2	111.8±2.2	192.9
U69	1day 5hr	45° to 75°	53.0±1.6	143.4±3.2	196.4
U70	13min 39s	70° to 80°	374.8±9.4	65.8±1.2	440.6
U70	3hr 54min	70° to 80°	428.7±16.1	110.5±2.4	539.2

oxide (z). This ratio is given by

$$\frac{z'}{z} = \frac{a + 1}{a} \frac{D_{\text{metal}}}{D_{\text{oxide}}} \quad (3.1)$$

where a is the ratio of the mass of the metal atoms to the mass of the oxygen atoms in the oxide, and D is the density for either the metal or the oxide. This assumes that all the expansion due to oxidation is in one dimension, i.e. there is no buckling or cracking, etc. It also assumes that the density of the bulk is the same as that of the thin films. For uranium dioxide the mass of one mole of uranium 238 g and the mass of one mole of oxygen is 32 g. So a is given by

$$a_{UO_2} = \frac{\text{molar mass of U}}{2(\text{molar mass of O})} = \frac{238}{2(16)} = 7.44 \quad (3.2)$$

The density of uranium is 18.9 g/cm³, and the density of uranium dioxide is 10.8 g/cm³ [33]. This gives an expansion ratio of

$$\frac{z'}{z} = \frac{(7.44 + 1)}{7.44} \frac{18.9}{10.9} = 1.97. \quad (3.3)$$

For comparison Table 3.3 gives the expansion ratio calculated this way for a number of different uranium oxides.

To transform an oxidation rate in units of mg/cm²/h (r_{mass}) to an oxidation rate in units of Å/s ($r_{\text{thickness}}$) the following formula is used:

$$r_{\text{thickness}}[\text{Å/s}] = \frac{(a + 1)}{D_{\text{oxide}}} \frac{1000}{36} r_{\text{mass}}[\text{mg/cm}^2/\text{h}]. \quad (3.4)$$

Here the density (D_{oxide}) is assumed to have units of g/cm³. If the original units of r_{mass} were in minutes instead of hours then the 36 in the denominator would be

Table 3.3: Expansion ratios of different uranium oxides.

Oxide	Density [33]	Molar Mass	a	Expansion Ratio
UO ₂	10.96	270	7.44	1.97
U ₃ O ₈	8.30	842	5.58	2.70
UO ₃	7.29	286	4.96	3.13

replaced with 0.6. This equation assumes that all the mass gain is due to accumulation of oxygen. It is not applicable when there is mass lost due to the oxide being volatile.

3.3.2 Previous Work

There have been many studies conducted on the rate and mechanisms of uranium oxidation. For a good overview of these studies consult references [34, 35, 36]. These references outline variations in the oxidation rate of uranium over temperature, water vapor pressure, oxygen partial pressure, carbon monoxide partial pressure and impurity concentrations. McGillivray, *et al.* have taken the data from previous studies and combined it with their own to develop an equation for variations of oxidation rate over a wide range of temperatures and water vapor pressures [37]. The equation they developed is

$$\text{oxidation rate in units of mg/cm}^2/\text{h} = \frac{k_1 P}{1 + k_2 P} + D, \quad (3.5)$$

where D , k_1 and k_2 are defined as follows, $T(K)$ is the temperature in Kelvin.

$$\ln D = 11.093 - \frac{8077}{T(K)} \quad (3.6)$$

$$\ln k_1 = 7.831 - \frac{6432}{T(K)} \quad (3.7)$$

$$\ln k_2 = -15.208 + \frac{5327}{T(K)} \quad (3.8)$$

Most of the data used to develop this equation was for high temperatures (above 115°C). However, if it is applied at room temperature it gives a rate of about 0.35 Å/hour with 10kPa water vapor partial pressure. Citations for measurements of the oxidation rate near room temperature are not common. Ritchie *et al.* measured a rate at 50°C in dry air of about 46 Å/hour [38]. With this higher temperature, a faster rate is expected, but for general considerations 0.35 to 46 Å/hour gives a range of possible values for the oxidation rate at room temperatures. All of these studies have used bulk samples that have been mechanically and/or chemically cleaned before oxidation is allowed to take place. As far as I know there have been no studies that have shown any dependency of the rate on time nor have there been any studies on the oxidation rate of sputtered thin films of uranium. Tench [39] showed a slower oxidation rate of thin films of uranium grown with laser ablation as compared to bulk rates. However, his study did not specifically address the value of the oxidation rate.

3.3.3 Ellipsometry Measurements

Sputtered thin films often behave differently than bulk samples. There is little data about room temperature oxidation of uranium. For this reason a study of room temperature oxidation of sputtered uranium thin films was conducted. Ellipsometry was used to determine oxide and unoxidized uranium thicknesses for four different

uranium thin films. The films were D.C. magnetron sputtered. Measurements began as soon as possible after removing the films from vacuum. Measurement times after removing from vacuum varied from 7 minutes to 23 days. A summary of the data is found in figure 3.15. Variations in roughness between samples as well as uncertainty in optical constants make the exact values for thicknesses questionable. However, the rate of change in thicknesses over time is more reliable. This can be seen by looking at the graph in figure 3.15. The data shows two sets of points. One below the fit line and one above. The slope of each of these sets is the same and is given by

$$\text{rate } [\text{\AA}/\text{S}] = \frac{d}{dt}(12.52 \ln(t) - 31) = \frac{12.52}{t} \quad (3.9)$$

This rate varies with time, unlike the rates previously quoted in the literature. It is difficult to say the range of time where this function is applicable. Obviously it is not applicable at the very beginning stages of oxidation. If the thin film is thick enough it could reach a critical point when the oxide layer begins to flake off and allow faster oxidation of the uranium below it. If this was the case the rate would reach a steady state value until all of the uranium was oxidized. There are many different mechanisms that can give a logarithmic rate equation like the one found here [40]. Determining which of these is most credible is beyond the scope of this research.

Using the ratio of the change in uranium thickness to the change in oxide thickness an expansion ratio was calculated. If all the data was used a value of about 1 is found for the expansion ratio, but the standard deviation for this value is 2.6. This large standard deviation is primarily due to inaccuracy in determining the thickness of the non-oxidized uranium layer. It was not uncommon to see the thickness of this uranium

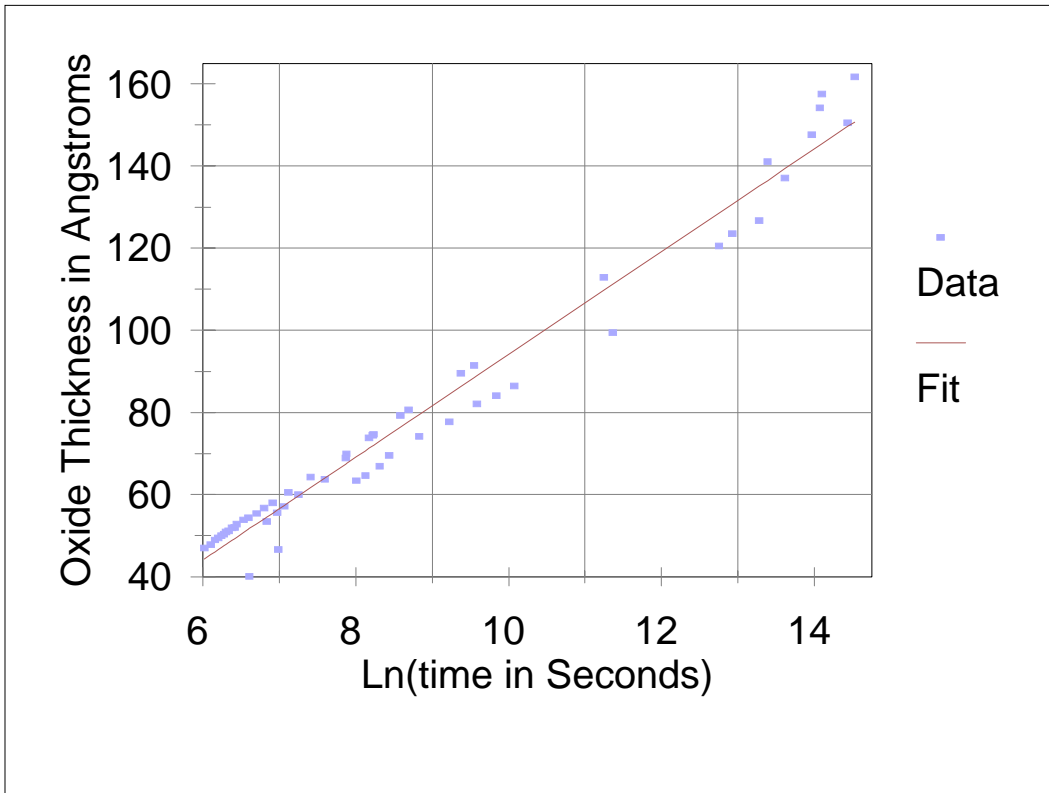


Figure 3.15: Uranium Oxidation Data and Fit: $y = 12.5x - 31$ $x = \ln t$.

layer, found from fitting ellipsometry data, to grow with time. If the outlying and unreasonable values for change in the uranium thickness are thrown out, an expansion ratio of 1.3 is obtained with a standard deviation of 0.55. Although this number is still below any of the expansion ratios in Table 3.3, it is closest to the expansion ratio for UO_2 . There are many reasons why it may be too low. The first and most likely reason is error in determining uranium thicknesses. It also could be due to differences between thin film and bulk values of the density for uranium and uranium oxide.

Chapter 4

Conclusion

Uranium is a promising material for making mirrors for the EUV. The success of the mirrors for the IMAGE mission is a good example. However, oxidized uranium can compromise the optical performance of uranium multilayers. The uranium oxygen water vapor system is very complicated. Greater understanding of this system is necessary to accurately design mirrors with uranium. This work has shown a dramatic difference in the oxidation rate of sputtered uranium thin films as compared to bulk uranium. It has shown that uranium thin films oxidize to UO_2 but that there can be hyperstoichiometric layers on the surface. In the process of studying uranium thin films a new way of analyzing X ray diffraction data was developed. This new information and tool should significantly aid in the design of multilayer thin films.

This new method for analyzing X ray diffraction data was developed by considering the Γ , d-spacing, merit function surface. This new method uses modified data and compares it to calculated values with the Pearson's correlation coefficient. This

method makes it easier to determine the d-spacing and Γ values for multilayers. It also shows promise in allowing aperiodic multilayers to be characterized with X ray diffraction. Further research needs to be conducted to see what kind of information can be obtained this way.

XPS data has shown that uranium oxidizes to uranium dioxide at standard temperature and pressure. It was previously thought that it oxidized to uranium trioxide [3]. The very surface of the oxide is not pure uranium dioxide. There is either a higher oxide or a hydroxide or both that develop on the surface. Exactly which and what role this surface layer plays in the optical properties of the multilayer is a topic of further research. Depth profiling with XPS has shown that silicon may play a part in stopping the oxidation from progressing further down into the stack. This could also be an subject of additional research.

Oxidation rates for thin films of sputtered uranium were found to vary with time according to the equation

$$\text{rate } [\text{\AA}/\text{S}] = \frac{12.52}{t}. \quad (4.1)$$

Knowing this is useful in the design and production of uranium thin films. It would also be valuable to better understand the oxidation mechanism that produces this time dependant rate. By understanding this mechanism it would be easier to find ways of stopping or slowing down the oxidation process.

This work has answered many questions about the composition and structure of the uranium oxide cap. However, there is much work to be done to determine the effects this top layer has on reflectance. The new XRD analysis tool shows promise

for determining additional information about a sample with X ray diffraction data. It is difficult to tell just how much information can be gained this way. Further research into this field could be enlightening. The dramatic difference in oxidation rates of sputtered uranium thin films to that of bulk uranium merits further research in this area as well. As in most scientific research, while seeking after answers many more questions arise.

Appendix A

XRD $P_c(d_1, d_2)$ Surface plots

This appendix contains three surface plots generated with the new XRD data analysis tool as describe in section 2.1.4. The first two plots were made with XRD data that had been calculated from a hypothetical multilayer. The last plot is an example of the limitations of this method. This is a plot made with XRD data taken from a ruthenium/aluminum 4 period multilayer. It is difficult to determine the correct d-spacing or the correct Γ with this plot. However, it was also difficult to determine these parameters with the traditional method as describe in section 2.1.3.

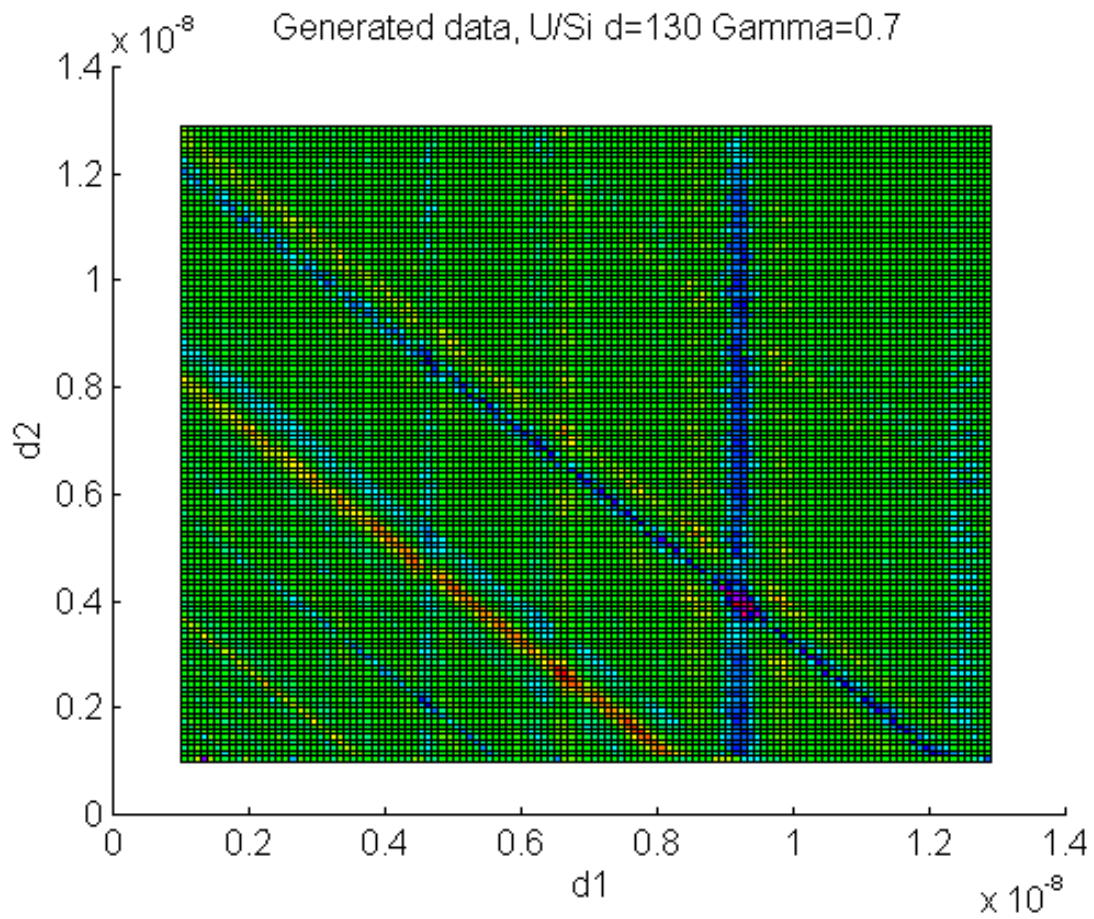


Figure A.1: d_1 and d_2 space for a hypothetical multilayer with a d-spacing of 130 Å and a Γ of 0.7.

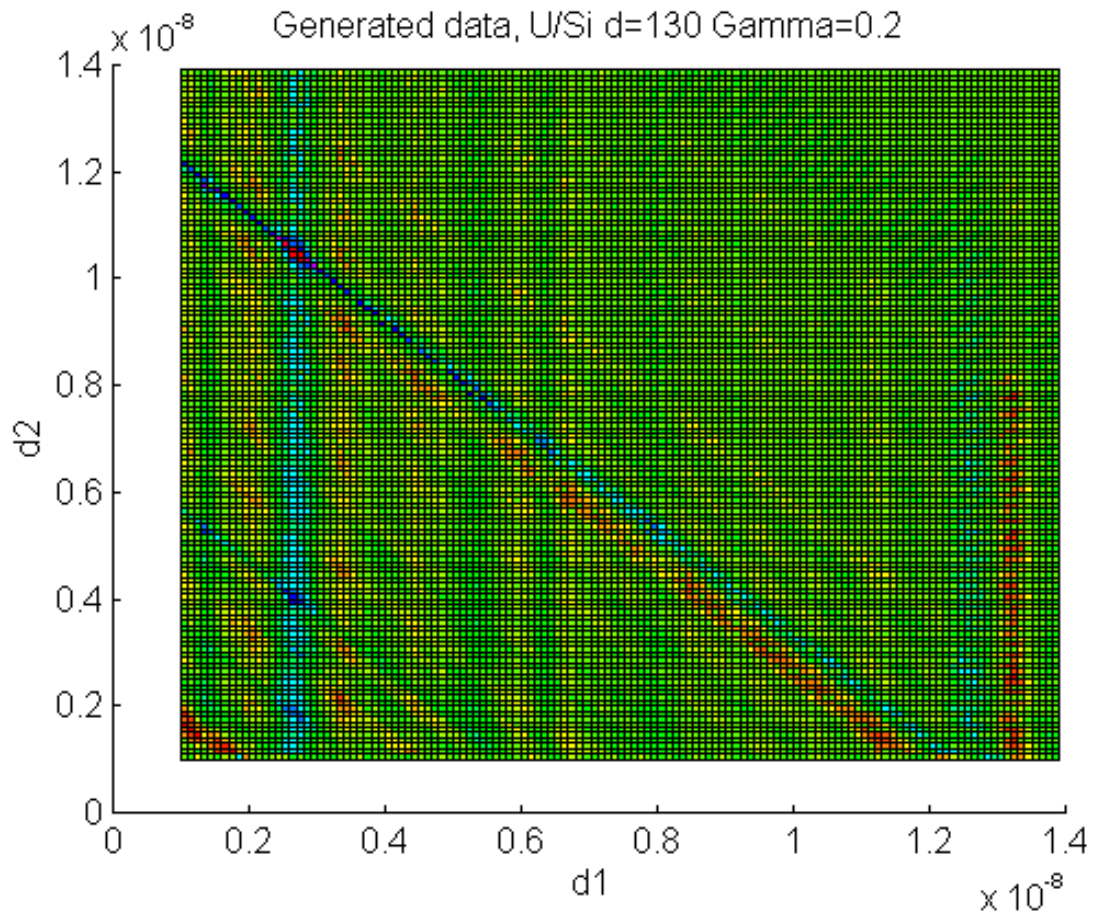


Figure A.2: d_1 and d_2 space for a hypothetical multilayer with a d-spacing of 130 Å and a Γ of 0.2.

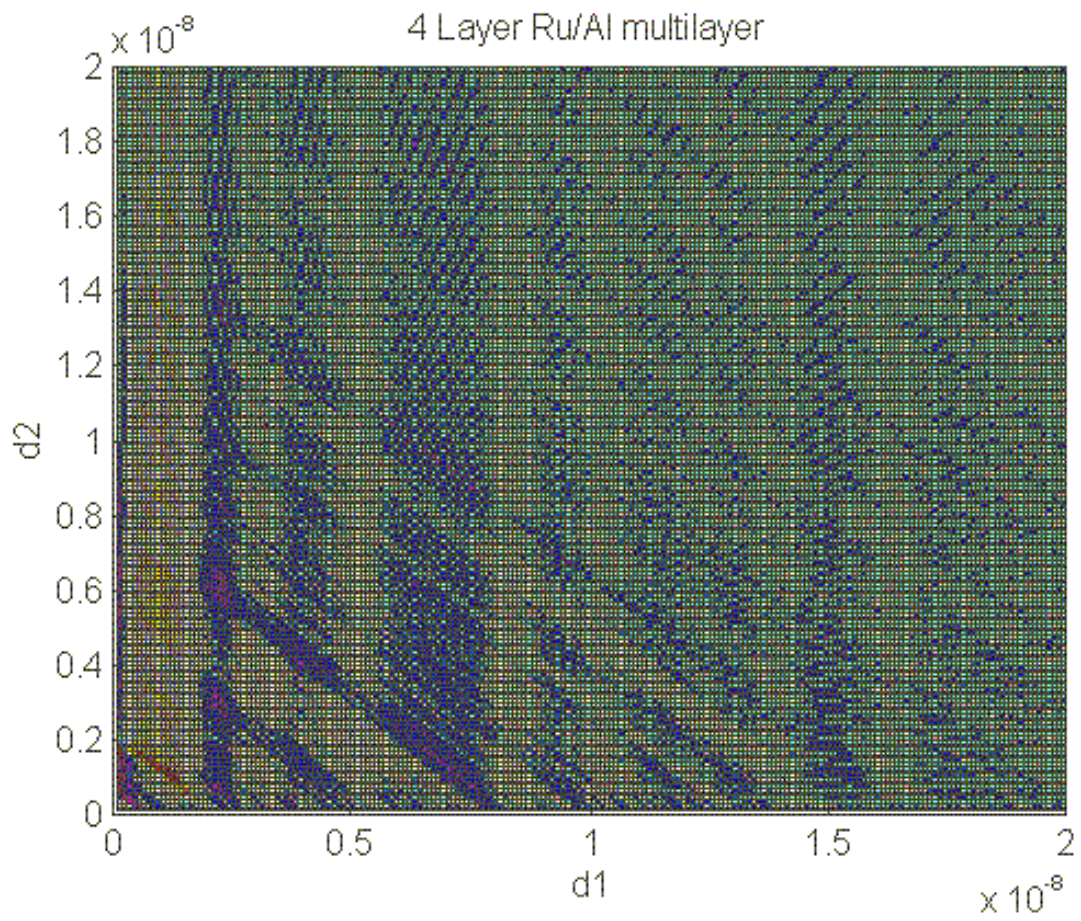


Figure A.3: d_1 and d_2 space for a ruthenium/aluminum multilayer with 4 periods.

Bibliography

- [1] EUV Team Members. Web site :
http://pluto.space.swri.edu/IMAGE/EUV_team.html, August 11, 2000.
- [2] B.R. Sandel, *et. al.* The Extreme Ultraviolet Imager Investigation for the IMAGE Mission. Space Science Reviews, IMAGE special issue. **91** (February, 2000.) 197-242, Obtained on the web site: <http://euv.lpl.arizona.edu/euv/index.html>.
- [3] Matthew B. Squires. On Determining the Optical Constants of Sputtered U and a-Si at 304 and 584 Å. Honors Thesis, BYU Physics Department. March 1999.
- [4] Shannon Lunt. The Use of Genetic Algorithms in Multilayer Mirror Optimization. Honors Thesis, BYU Physics and Astronomy Department. March 1999.
- [5] Adam Fennimore. Morphology and Oxidation of U/Al and UN/Al Multilayer Mirrors. Honors Thesis, BYU Physics and Astronomy Department. 1998.
- [6] David D. Allred and R. Steven Turley. Mirror Design, Fabrication and Testing. Brigham Young University. May 24, 1999.
- [7] David John Jackson. *Classical Electrodynamics Third Edition*. John Wiley and Sons, Inc. New York. 1999.
- [8] Grant R. Fowles. *Introduction to Modern Optics, Second Edition*. Dover Publications, Inc., New York. 1975.
- [9] Max Born and Emil Wolf. *Principles of Optics, Electromagnetic Theory of Propagation, Interference and Diffraction of Light, Seventh (Expanded) Edition*. Cambridge University Press, Cambridge, United Kingdom. 1999.
- [10] David Windt. IMD - Software for Modeling the Optical Properties of Multilayer Films. Computers in Physics. **12** no. 4 (July/Aug 1998) 360-70.
- [11] Jean M. Bennett and Lars Mattsson. *Introduction to Surface Roughness and Scattering, Second Edition*. Optical Society of America. 1999.
- [12] D. G. Stearns. The Scattering of X-rays From Non-ideal Multilayer Structures. Journal of Applied. Physics. **65** (15 January 1989) 491.

- [13] Harold T. Stokes. *Solid State Physics, for Advanced Undergraduate Students*, third edition, second printing. Brigham Young University. 1998.
- [14] R. Steven Turley. Software written at Brigham Young University. July 3, 1999
- [15] J.A. Woollam Help files for the software: WVASE32. A Short Course in Ellipsometry/Regression Analysis of Optical Data.
- [16] Milton Ohring. *The Materials Science of Thin Films*. Academic Press, Inc., San Diego, 1992.
- [17] Suli Suder, C.A. Faunce and S.E. Donnelly. Two-View Small-Angle Wedge Sample Preparation By Hand Tools for Transmission Electron Microscopy of Semiconductors and Related Materials. MRS Symposium Proceedings. **480** (April 1997) 73 .
- [18] P. J. Goodhew. *Specimen Preparation in Materials Science*. North-Holland Publishing Company. pg. 38. 1972.
- [19] Scott D. Walck and John P. McCaffrey. The Small Angle Cleavage Technique: An Update. MRS Symposium Proceedings. **480** (April 1997) 149.
- [20] An Introduction to XPS - X-ray Photoelectron Spectroscopy. Web site: <http://www.ukesca.org/tech/xps.html>. ESCA Users Group Surface Science Site, 1998.
- [21] BE Lookup Table for Signals from Elements and Common Chemical Species, *Handbook of the Elements and Native Oxides*. XPS International, Inc. 1999. Obtained on the web.
- [22] Index of Refraction. Web site: http://www-cxro.lbl.gov/optical_constants/getdb2.html. Center for X-Ray Optics, Materials Science Division, Lawrence Berkeley National Lab. 2000
- [23] Yu.A. Teterin, *et. al.* A Study of Synthetic and Natural Uranium Oxides by X-ray Photoelectron Spectroscopy. *Physics and Chemistry of Minerals*, Springer-Verlag 1981, pg 151.
- [24] M.N. Hedhili, B.V. Yakshinskiy and T. E. Madey. Interaction of Water Vapor With UO_2 . *Surface Science*. **445** (2000) 512-525
- [25] Jennifer McBride, personal correspondence, X-Ray Photoelectron Spectrometer Technician at the University of Utah, 30 May 2000.
- [26] A.Fäldt and P.O. Nilsson, Optical Properties of uranium in the range 0.6 - 25 eV. *J. Phys. F: Metal Phys.* **10** (1980) 2573.

- [27] R.J. Ackermann, R.J. Thorn and G.H. Winslow. Visible and Ultraviolet Absorption Properties of Uranium dioxide Films. *Journal of the Optical Society of America*. **49** no.11 (November 1959) 1107.
- [28] J.L. Bates. Visible and Infrared Absorption Spectra of Uranium Dioxide. *Nuclear Science and Engineering*. **21** (1965) 26-29.
- [29] J. Schoenes. Optical Properties and Electronic Structure of UO_2 . *J. Appl. Phys.* **49** no. 3 (March 1978) 1463.
- [30] Trevor R. Griffiths, Hugh V.St.A. Hubbard, Geoffrey C. Allen and Paul A, Tempest. A New Method for the Determination of x in UO_{2+x} : Optical Absorption Spectroscopy Measurements. *Journal of Nuclear Materials* **151** (1988) 307-312.
- [31] J. Naegele, L. Manes and U. Birkholz. Optical Properties of UO_2 and U_4O_9 Single Crystals and Their Relation to Chemical Bonding. *Plutonium and Other Actinides*. 1976. pg 393.
- [32] C.M. Herzinger, B Hohn, W.A. McGahan, J.A. Woollam and W. Paulson. Ellipsometric determination of optical constants for silicon and thermally grown silicon dioxide via a multi-sample, multi-wavelength, multi-angle investigation. *Journal of Applied Physics*. **83** no. 6 (15 March1998) 3323.
- [33] David R. Lide Editor-in-Chief, *CRC Handbook of Chemistry and Physics 75th Edition*. CRC press, Ann Arbor, 1994.
- [34] C.A. Colmenares. Oxidation Mechanisms and Catalytic Properties of the Actinides. *Progress in Solid State Chemistry*, **15** (1985) 257.
- [35] Lawrence J. Korb, David L. Olson. Co-Chairmen. *Metals Handbook, Ninth Edition, Volume 13 Corrosion*. ASM International 1987.
- [36] K.A. Winer, Initial Stages of Uranium Oxidation: A Surface Study. Ph. D. Thesis, Lawrence Livermore National Laboratory. July 1, 1985.
- [37] G.W. McGillivray, D.A. Geeson and R.C. Greenwood. Studies of the Kinetics and Mechanism of the Oxidation of Uranium by Dry and Moist Air, A Model for Determining the Oxidation Rate Over a Wide Range of Temperatures and Water Vapor Pressures. *Journal of Nuclear Materials*. **208** (1994) 81-97.
- [38] A.G. Ritchie, R.C. Greenwood and S.J. Randles, *Journal of Nuclear Materials*. **139** (1986) 121.
- [39] Robert John Tench, The Nucleation and Growth of Uranium on the Basal Plane of Graphite Studied by Scanning Tunneling Microscopy. Ph.D. Thesis, Lawrence Livermore National Laboratory, November 1992.
- [40] Per Kofstad. *High-Temperature Oxidation of Metals*. John Wiley & Sons, Inc. New York.1966.